JrnlID 10494_ArtID 9866_Proof#1 - 14/10/2017

Flow Turbulence Combust
https://doi.org/10.1007/s10494-017-9866-2

LES-based Study of the Roughness Effects on the Wake of a Circular Cylinder from Subcritical to Transcritical Reynolds Numbers

Ivette Rodriguez[1] · Oriol Lehmkuhl[1,2] · Ugo Piomelli[3] · Jorge Chiva[4] · Ricard Borrell[4] · Assensi Oliva[4]

Received: 1 March 2017 / Accepted: 10 October 2017

Abstract This paper investigates the effects of surface roughness on the flow past a circular cylinder at subcritical to transcritical Reynolds numbers. Large eddy simulations of the flow for sand grain roughness of size $k/D = 0.02$ are performed (D is the cylinder diameter). Results show that surface roughness triggers the transition to turbulence in the boundary layer at all Reynolds numbers, thus leading to an early separation caused by the increased momentum deficit, especially at transcritical Reynolds numbers. Even at subcritical Reynolds numbers, boundary layer instabilities are triggered in the roughness sublayer and eventually lead to the transition to turbulence. The early separation at transcritical

Q1 ✉ Ivette Rodriguez
ivette.rodriguez@upc.edu

Oriol Lehmkuhl
oriol.lehmkuhl@bsc.es

Ugo Piomelli
ugo@queensu.ca

Jorge Chiva
Q2 jordic@cttc.upc.edu

Ricard Borrell
ricardb@cttc.upc.edu

Assensi Oliva
oliva@cttc.upc.edu

[1] Universitat Politècnica de Catalunya (UPC), Colom 11, ESEIAAT, 08221 Terrassa, Spain

[2] Barcelona Supercomputing Centre (BSC), Barcelona, Spain

[3] Department of Mechanical and Materials Engineering, Queen's University, Kingston, Ontario K7L 3N6, Canada

[4] Centre Tecnològic de Transferència de Calour (CTTC), Universitat Politècnica de Catalunya (UPC), Barcelona, Spain

JrnlID 10494_ArtID 9866_Proof#1 - 14/10/2017

Reynolds numbers leads to a wake topology similar to that of the subcritical regime, resulting in an increased drag coefficient and lower Strouhal number. Turbulent statistics in the wake are also affected by roughness; the Reynolds stresses are larger due to the increased turbulent kinetic energy production in the boundary layer and separated shear layers close to the cylinder shoulders.

Keywords LES · Vortex shedding · Wakes · Roughness

1 Introduction

Surface roughness is present in many engineering applications and its effects on turbulent boundary layers are of interest in aerodynamics, turbo-machinery, the earth sciences, and other disciplines. The effect of roughness has been the focus of much research (see for instance [1–3]). Most of the investigations in this area, however, have been performed on fully developed turbulent pipes and channels, and in zero-pressure-gradient turbulent boundary layers. In the particular case of cylinders, roughness may cause early transition from laminar to turbulent flow in the boundary layer, and may also change the way the flow develops behind the cylinder (see for instance [4]).

In the flow past smooth circular cylinders, different flow regimes can be observed depending on the boundary layer behaviour. According to [5] there are four regimes: subcritical with laminar separation, critical with a rapid decrease in the drag coefficient and the formation of an asymmetric laminar separation bubble (LSB), supercritical with a plateau in the drag and two symmetric LSBs followed by turbulent separation, and transcritical, where separation is purely turbulent. A detailed description of these flow regimes can be found in the review by [6]. Considerable work has been carried out measuring flow parameters (drag and lift coefficients, non-dimensional vortex shedding frequency, amongst others) at the different Reynolds numbers, and in particular, in the critical and supercritical regimes (see for instance [4, 7–12]).

Similar regimes were defined for the rough cylinder by [13], based on his drag measurements (see Fig. 1). In the subcritical regime, the boundary layer is not influenced by the roughness. With the increase in the Reynolds number, the flow enters the critical regime and there is a drop in the drag coefficient: the onset of the critical transition is shifted to lower Reynolds numbers [14] as the roughness height increases, but the minimum drag coefficient is larger than that on a smooth cylinder, due to the transition to turbulence occurring at lower Reynolds numbers, and to an earlier separation due to the increased drag (and momentum deficit) caused by the roughness [13, 15–17]. The region between the minimum drag coefficient and the zone where the Reynolds number reaches a plateau is the supercritical regime; in the transcritical regime the drag remains constant, independent of the Reynolds numbers.

The shift in the critical regime to lower Reynolds numbers is documented by the experiments of [15] and was later confirmed by other experiments such as those conducted by [13]. [18] measured the pressure distributions on smooth and rough cylinders in both uniform flow and turbulent stream in the critical regime, and discovered that pressure distribution and separation point can be changed due to the effects of roughness and inlet turbulent levels.

Pressure distributions and boundary layer development on rough cylinders were also measured by [16]. Achenbach's (1971) observations on the drag coefficient independence on the Reynolds number in the transcritical regime are confirmed by their work. Moreover, increase of the roughness size is seen to lead to a thicker boundary layer with early

JrnlID 10494_ArtID 9866_Proof#1 - 14/10/2017

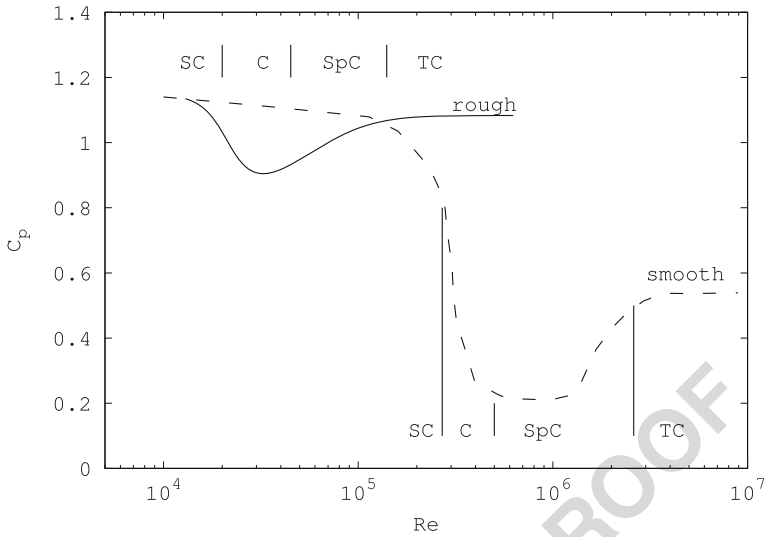

Fig. 1 Flow regimes in the flow past rough and smooth cylinders. SC - subcritical, C - critical, SpC supercritical, TC - transcritical

separation and smaller pressure recovery. Also, in agreement with [13], the influence of roughness on the flow regime and the reduction of the minimum drag as the roughness size increases is confirmed by [19]. [20] observe that roughness causes early transition, but also that using localised roughness a drag coefficient lower than that of the distributed roughness can be obtained in the transcritical regime. Mean and fluctuating forces on different types of rough surfaces were measured by [21, 22]. In his studies, all roughness types triggered early transition to turbulence, ribs being more efficient at reducing the drag coefficient.

More recently, other type of surfaces, such as grooved cylinders, have been the focus of investigations. For instance, [23] performed experiments on the influence of V-grooved micro-riblet films on the drag coefficient for a circular cylinder at low Reynolds numbers. However, whether this is beneficial can not be determined from their experiments as reductions in the drag coefficient of 7% are found at $Re = 3.6 \times 10^3$ but increases 4% at $Re = 3.6 \times 10^4$. In contrast, [24] test different cylinders with grooved surface and report a considerable drag reduction when compared to the smooth cylinder, in most of the cases.

Most of the experimental studies carried out so far focus on mean forces and vortex shedding measurements, whilst quantitative studies of the flow field, including measurements of the mean and fluctuating quantities around the rough cylinder are scarce. The present work pays particular attention to how the changes roughness introduces in the boundary layer affect the transition to turbulence and, as a consequence, the flow conditions behind the cylinder. To do this, the flow past a rough cylinder at a Reynolds numbers of $Re = 3.0 \times 10^4$, 4.2×10^4 and 4.2×10^5 with a sand-grain surface with roughness height $k \simeq 0.02D$ is studied by means of large-eddy simulations (LES). According to [13], these Reynolds numbers should correspond to subcritical, critical and transcritical flow regimes, respectively. Thus, changes due to surface roughness in the flow parameters, boundary layer and flow topology behind the cylinder can be analysed for the different regimes and by means of the direct comparison with available results for the smooth cylinder.

JrnlID 10494_ArtID 9866_Proof#1 - 14/10/2017

2 Mathematical and Numerical Models

The spatially filtered incompressible Navier-Stokes equations [25] can be written as

$$\frac{\partial \overline{u}_i}{\partial x_i} = 0 \tag{1}$$

$$\frac{\partial \overline{u}_i}{\partial t} + \frac{\partial \overline{u}_i \overline{u}_j}{\partial x_j} - \nu \frac{\partial^2 \overline{u}_i}{\partial x_j \partial x_j} + \rho^{-1} \frac{\partial \overline{p}}{\partial x_i} - F_i = -\frac{\partial \mathcal{T}_{ij}}{\partial x_j} \tag{2}$$

where x_i are the spatial coordinates (or x, y, and z) in the stream-wise, cross-stream and span-wise directions. $\overline{u}_i$ (or $\overline{u}$, $\overline{v}$, and $\overline{w}$) stand for the filtered velocity components and $\overline{p}$ is the pressure. ν is the kinematic viscosity and ρ the density of the fluid. F_i is a body force used to impose the no-slip boundary condition on the rough cylinder surface; it is non-zero only in the cells including part or all of a roughness elements [26]. In Eq. 2 $\mathcal{T}_{ij}$ is the subgrid scale (SGS) stress tensor, which must be modelled. Its deviatoric part is given by

$$\mathcal{T}_{ij} - \frac{1}{3}\mathcal{T}_{kk}\delta_{ij} = -2\nu_{sgs}\overline{\mathcal{S}}_{ij} \tag{3}$$

where $\overline{\mathcal{S}}_{ij} = \frac{1}{2}\left(g_{ij} + g_{ji}\right)$ is the large-scale rate-of-strain tensor, and $g_{ij} = \partial \overline{u}_i / \partial x_j$. δ_{ij} is the Kronecker delta. The formulation is closed by an appropriate expression for the subgrid-scale viscosity, ν_{sgs}. In this project the wall-adapting local-eddy viscosity model (WALE) [27] is used. This model yielded good results in previous simulations of the smooth cylinder at critical and supercritical Reynolds numbers (see [9] and [10]).

The governing equations are discretised on a collocated unstructured grid arrangement using second-order spectrum-consistent schemes. Such schemes are conservative, i.e., the symmetry properties of the continuous differential operators are preserved, and both stability and conservation of the kinetic-energy are ensured, even at high Reynolds numbers and with coarse grids [28, 29]. A self-adaptive two-step linear explicit scheme on a fractional-step method for the convective and diffusive terms [30] is used for the temporal discretisation of the momentum equation, whilst an implicit first-order scheme is implemented for the pressure gradient. For more details about the numerical method, the user is referred to [28, 29, 31].

An immersed boundary method (IBM) is used to recover a smooth no-slip boundary condition on the rough cylinder surface. It is based on the volume-of-fluid approach, i.e., the volume fraction occupied by the fluid of each cell is used in the fractional-step framework to correct the predicted velocity and enforce the no-slip condition on the rough surface. For more details the reader is referred to [26, 32, 33]. To represent the roughness, following the model proposed by [32] , the cylinder surface is divided into $n_\theta \times n_z$ cells of side $2k/D$. Within each cell, randomly rotated ellipsoids with semi-axes k/D, $1.4k/D$ and $2k/D$ are placed (k is the roughness height, see Table 1). At the Reynolds numbers of the present calculations, this model results in an equivalent sand-grain roughness $k_s/D \simeq 0.02 - 0.03$ [34]. The volume fraction for a given mesh and roughness height is then calculated once during pre-processing. It is important to stress that this sandgrain model produces a 'grey' interface between the roughness and the fluid whose location ~~depend~~ on the grid size. However, as discussed in [26], the flow around a roughness element is not the focus for the fluid application under study and thus, this treatment does not affect greatly the statistics of the roughness sublayer and the cylinder wake.

JrnlID 10494_ArtID 9866_Proof#1 - 14/10/2017

Table 1 Summary of simulation parameters

mesh	NCV_{plane}	N_{planes}	$NCV_{total} \times 10^{-6}$	L_z	Δ_z	Δ_r^{3k}	$N_z \times N_\theta$	$n_z \times n_\theta$	n_r^{3k}
M0	217594	192	41.77	0.96	5×10^{-3}	2×10^{-3}	24×78.5	8×8	30
M1	285658	384	109.7	0.96	2.5×10^{-3}	1.22×10^{-3}	24×78.5	16×16	50
M2	343846	480	165	0.96	2×10^{-3}	10^{-3}	24×78.5	20×20	60
M3	217594	384	83.5	1.92	5×10^{-3}	2×10^{-3}	48×78.5	8×8	30
M4	285658	768	219.4	1.92	2.5×10^{-3}	1.22×10^{-3}	48×78.5	16×16	50
M5	217594	768	167.1	3.84	5×10^{-3}	2×10^{-3}	96×78.5	8×8	30
M6	285658	1536	438.8	3.84	2.5×10^{-3}	1.22×10^{-3}	96×78.5	16×16	50

NCV_{total} is the total number of control volumes; NCV_{plane} is the total number of control volumes in the plane; N_{planes} is the total number of planes in the span-wise direction; L_z is the span-wise size of the domain; Δ_z, Δ_r^{3k} are the span-wise resolution and wall-normal resolution within a distance of $3k/D$; N_θ, N_z are the total number of sandgrain elements; n_θ, n_z are the average mesh resolution for each roughness element; n_r^{3k} is the number of grid points in the wall normal direction within a $3k/D$ distance

JrnlID 10494_ArtID 9866_Proof#1 - 14/10/2017

The Poisson system derived from the incompressibility constraint is solved using a memory-aware auto-tuned Poisson solver for problems with one Fourier diagonalizable direction. This diagonalization decomposes the original 3D system into a set of independent 2D subsystems. The algorithm focuses on optimising the memory allocations and transactions by taking into account redundancies on such 2D subsystems. Moreover, it takes advantage of the grid uniformity in the periodic direction for its vectorisation. This approach automatically optimises the choice of the preconditioner used for the solution of each frequency subsystem and dynamically balances its parallel distribution, constituting a highly efficient and robust HPC Poisson solver. This strategy allows to involve larger number of parallel processes in a single task, with less RAM memory per parallel process [35, 36].

2.1 Definition of the case and boundary conditions

The flow past a rough circular cylinder at Reynolds numbers $Re = 3 \times 10^4$, 4.2×10^4, 4.2×10^5 with a sand-grain surface with height $k/D \simeq 0.02$ is considered. Here, the Reynolds number $Re = U_{ref}\ D/\nu$ is defined in terms of the cylinder diameter D and the free-stream velocity U_{ref}. As the value of the surface roughness is quite high ($k/D \simeq 0.02$) it would be interesting to analyse how roughness affect the wake at these different Reynolds numbers and if the regimes observed by [13] here apply. Also note that for the smooth cylinder the first two Reynolds numbers correspond to the subcritical regime, whereas the last one is in the critical regime (see for instance [9, 10, 13]).

The cases are solved in a computational domain of dimensions $x \equiv [-10D : 20D]$; $y \equiv [-10D : 10D]$ in the stream-wise and cross-stream directions and three different span-wise lengths of $0.96D$, $1.92D$ and $3.84D$, with a circular cylinder of diameter D at (0, 0, 0). The dimensions of the domain in the stream-wise and cross-stream directions must be sufficient to contain the largest structures and allow the flow on the cylinder to be unaffected by the boundary conditions. This is especially true for the cross-stream direction where symmetry conditions are prescribed. Since the boundary does not allow fluxes to cross, the boundary should be placed far from the cylinder surface. In this work it is placed at a distance of 10D from the cylinder; both streamwise and cross-stream domain sizes have been proven to be sufficient in similar flows (see for instance [9, 10, 37, 38]). The boundary conditions at the inflow consist of a uniform velocity $(u, v, w) = (1, 0, 0)$. At the outlet, a pressure-based condition is used (see for instance [31]. In the span-wise direction periodic boundary conditions are imposed.

At the cylinder surface, as commented previously a virtual sandpaper is used to impose the roughness [26, 32, 33]. A detail of the resulting sand-grain roughness surface is shown in Fig. 2, where the visualisation of the fraction of volume $\phi = 0.5$ is shown, to represent the shape of the rough wall.

A two-dimensional unstructured grid with a constant step in the span-wise direction is extruded to obtain the three-dimensional mesh. A prism layer around the cylinder surface, extending up to the edge of the roughness sublayer, is constructed in the two-dimensional mesh. Beyond this distance from the wall an unstructured grid is used. [26] determined the maximum grid spacing required to represent this kind of surface roughness accurately. On this basis, in the present work, each roughness element is resolved by $n_\theta \times n_z$ cells (see Table 1) of the superficial mesh with $30 - 60$ points below the roughness crest in the wall-normal direction. Moreover, as the grid used is unstructured, more control volumes are clustered close to the cylinder and in the near wake, whereas away from the region of interest the mesh requirements are progressively relaxed (see Fig. 2b). Details about the meshes used are given in Table 1.

JrnlID 10494_ArtID 9866_Proof#1 - 14/10/2017

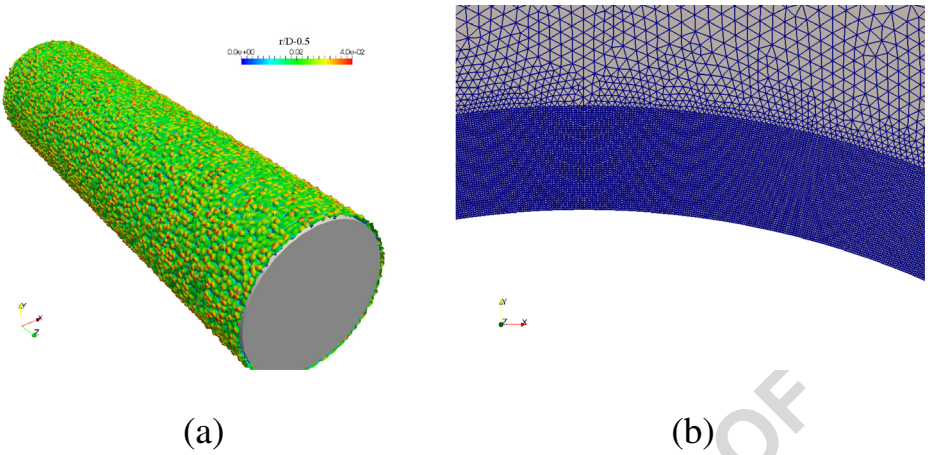

Fig. 2 **a** Visualisation of the sand-grain surface coloured by the height of the surface ($r/D - 0.5$, r is the radial distance from the cylinder centre). Note that in the figure the roughness is represented by the fraction of volume $\phi = 0.5$; **b** Detail of the mesh near the wall

2.2 Mesh sensitivity studies

As previously mentioned, three span-wise lengths and three levels of resolution of the roughness elements are considered here. In Table 2, the results of the drag coefficient, fluctuating drag and lift coefficients, minimum and base pressure coefficients, the location of the minimum pressure coefficient and the non-dimensional vortex shedding frequency are given for each of the meshes at $Re = 4.2 \times 10^4$.

The cases are simulated for a sufficiently long period of time to obtain converged statistics. For all simulations an initial transient period of roughly 60 time units ($TU = tU_{ref}/D$=60) is discarded, to ensure statistically steady state is reached and all transients have been washed out. After that, statistics are collected. In order to ensure this is sufficient integration time, the value of the averaged drag and lift fluctuations were also determined over the last half of the simulations. These values are within 1.2% of the value determined over the whole simulation, assuring well converged statistics.

Table 2 Flow parameters for different meshes at $Re = 4.2 \times 10^4$

mesh	C_D	$C_{D,rms}$	$C_{L,rms}$	$C_{p,min}$	θ_{min}	$-C_{pb}$	St	θ_{sep}
M0	1.29	0.099	0.516	−1.57	72.7	−1.422	0.206	87.3
M1	1.062	0.076	0.513	−1.74	73.1	−1.190	0.217	88.5
M2	1.073	0.076	0.531	−1.78	75	−1.234	0.222	87.0
M3	1.221	0.072	0.525	−1.40	74.7	−1.247	0.194	86.4
M4	1.074	0.059	0.411	−1.58	74.6	−1.15	0.211	88.5
M5	1.189	0.054	0.402	−1.44	73.3	−1.15	0.198	86.8
M6	0.994	0.041	0.316	−1.548	74.1	−1.024	0.214	87.5

C_D drag coefficient, $C_{D,rms}$ fluctuating drag, $C_{L,rms}$ fluctuating lift, $C_{p,min}$ minimum pressure coefficient, θ_{min} location of the minimum pressure coefficient, $-C_{pb}$ base pressure coefficient, St non-dimensional vortex shedding frequency and θ_{sep} separation angle

Roughness resolution has an important effect on the drag coefficient and on the base pressure. Note that the drag coefficient changes by 21.4% when roughness resolution is doubled for span-wise length of $L_z/D = 0.96$ (meshes M0 and M1), whilst for $L_z/D = 1.92$ the change in the drag coefficient is about 13.6%. On the other hand, the increase in the span-wise length of the domain greatly affects the fluctuating lift and drag coefficients. For instance, for surface roughness resolution of 16×16 doubling the span-wise size of the domain (meshes M4 and M6) represents a change in the fluctuating drag and lift of about 44% and 30.5%, respectively, whereas the change in the drag coefficient is 8%.

In general, both roughness resolution and span-wise size of the domain are important for the flow parameters. Analysing the results presented in Table 2 for the roughness resolution, at least a number of 16×16 grid points might be necessary to resolve each surface roughness sample. Regarding the span-wise length of the domain, it is not only related with the size of span-wise coherent structures that might be being truncated by a smaller length, but also with the number of surface roughness elements considered. An insufficient sampling might affect the distribution of the total drag on the surface as was shown by [26]. Thus, considering that both drag and fluctuating lift are affected by the randomness of the surface distribution, the larger the span-wise size of the domain, the larger the number of roughness samples considered and a better representation of the surface. For the sizes considered in Table 2, it seems that in terms of these quantities, there is still a large deviation if domain sizes of $L_z = 1.92D$ and $L_z = 3.84D$ are compared (meshes M4 and M6). However, in terms of wake statistics a span-wise length of $L_z = 3.84D$ should be enough to contain all relevant structures of the flow. The span-wise correlation was reported to vary as $\lambda_z/D = 20Re^{-0.5}$ at low Reynolds numbers [39]. In the range up to $Re = 2.1 \times 10^4$, it was observed to be $\lambda_z/D \approx 1$ irrespective of the Reynolds number [40], whereas in the critical regime it was measured around $\lambda_z/D \approx 1.4$ by [41] and lower than 1 by [9]. In order to ~~cheque~~ if $L_z = 3.84D$ is enough to accommodate larger structures, two-point correlations at different locations were evaluated. The one-dimensional two-point correlation of the fluctuating variable $\phi' = \phi - < \phi >$ is defined as

$$\Re_{\phi\phi}(x, y, \delta z) = \frac{\langle \phi'(x, y, z, t)\, \phi'(x, y, z + \delta z, t) \rangle}{\langle \phi'^2 \rangle} \tag{4}$$

where $\langle \cdot \rangle$ denotes averaging over time. In Fig. 3, two-point correlations at the cylinder apex $(x, y) \equiv (0.0, 0.54)$ and at the wake centreline $(x, y) \equiv (2, 0.0)$ are plotted for $Re = 3.0 \times 10^4$. In the location close to the cylinder apex, in the roughness sublayer, correlations drop to zero much faster than in the wake centreline, where larger structures are observed. Nonetheless, the spanwise length used seems to be acceptable for these Reynolds numbers.

In order to further analyse the effect of the span-wise size of the domain, the streamwise velocity and its fluctuations are plotted in Fig. 4 at $x/D = 0.97$ for $L_z = 1.92D$ and $L_z = 3.84D$. As can be seen from the figure, a fair agreement is found between the statistics for the two domain sizes, the largest differences being around 4% in the magnitude of the peaks. Owing to these results, in the present work the mesh $M6$ with a span-wise length of $L_z/D = 3.84$ and a roughness resolution of 16×16 grid points is used. A larger span-wise domain or finer roughness resolution would be preferable, but it was considered that the final mesh should be a trade-off between accuracy and computational effort required.

Finally, the resolution of the grid used in the simulations has been assessed by evaluating the ratio of the resolved scales to an estimate of the Kolmogorov length scale at each

JrnlID 10494_ArtID 9866_Proof#1 - 14/10/2017

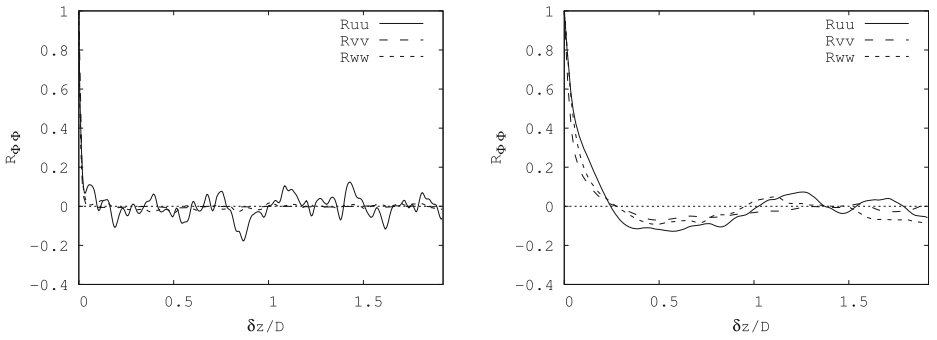

Fig. 3 One-dimensional two-point correlations at different locations **a** at $(x, y) \equiv (0.0, 0.54)$ and **b** at $(x, y) \equiv (2, 0.0)$ for $Re = 3.0 \times 10^4$

control volume. Here the Kolmogorov length scale is evaluated as $\eta = (\nu^3/\epsilon)^{1/4}$, where the turbulent kinetic energy dissipation rate is estimated as

$$\epsilon = (\nu + \nu_{sgs}) \overline{\frac{\partial u_i'}{\partial x_k} \frac{\partial u_i'}{\partial x_k}} \tag{5}$$

For the largest Reynolds number, i.e., $Re = 4.2 \times 10^5$, this ratio is of the order of 3 to 9 in the near wake, i.e. $x/D \leq 5$. According to [42] the motions responsible for the dissipation of a scale larger than that of the Kolmogorov scale ~~and~~ in the range of 8η to 60η, the peak of the dissipation of the turbulent kinetic energy occurs at approximately 24η. Thus, the grid used in the present work is capable of solving large part of the dissipation, indicative of the very good resolution achieved.

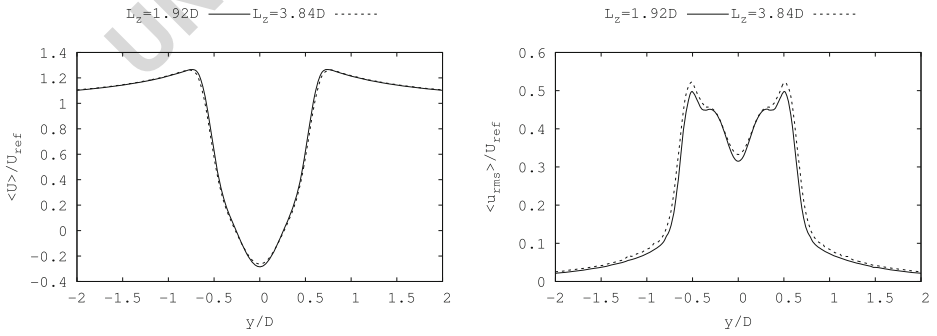

Fig. 4 Comparison of the wake statistics at $x/D = 0.97$ for two span-wise size of the domain. **a** stream-wise velocity and **b** stream-wise root-mean-square velocity

3 Results

As defined in Section 2.1, LES numerical simulations are performed on rough cylinders for three different Reynolds numbers of $Re = 3 \times 10^4,\ 4.2 \times 10^4,\ 4.2 \times 10^5$.

3.1 Flow parameters

The variation of the drag coefficient and the non-dimensional vortex shedding frequency with the Reynolds number is plotted in Fig. 5. For comparison, experimental data from [15] ($k_s/D = 2 \times 10^{-2}$ and $k_s/D = 9 \times 10^{-3}$), [13] ($k_s/D = 9 \times 10^{-3}$), [19] ($k_s/D = 1.2 \times 10^{-2}$) and [4] ($k_s/D = 3 \times 10^{-2}$ and $k_s/D = 9 \times 10^{-3}$) are also given in the figure. Note the large scattering between the different experiments, which makes a quantitative comparison difficult. This in part might be due to the different experimental arrangements used but also to the difficulties in estimating the effective size of the roughness elements. In most of the measurements, the reported values of k_s/D represent a rough estimate of the actual equivalent surface roughness [4, 16, 19]. Other experimental uncertainties reported are related to difficulties in the correction for wind tunnel blockage, end conditions issues caused by small gaps that produce some departure from ideal two-dimensional flow conditions, amongst others. A more complete discussion on the experimental conditions is given in Appendix A. In spite of the aforementioned issues, numerical results obtained are within the range of uncertainties reported and they seem to follow the same trend as experimental data. However, it would be convenient to analyse in more detail both the pressure distribution and the periodic behaviour of the forces acting on the cylinder surface.

The pressure coefficient distribution along the cylinder circumference for the different Reynolds numbers is shown in Fig. 6. For the two lower Reynolds numbers (i.e. $Re = 3 \times 10^4$ and $Re = 4.2 \times 10^4$) the pressure distribution is compared with the measurements for the smooth cylinder performed by [43]. They studied the effect of the cylinder aspect ratio and blockage and reported that for blockage larger than 6% considerable distortion of the flow might be observed, whereas for low aspect ratios both drag coefficient and base pressure are affected. Considering the foregoing, in this study experimental data for aspect ratio 10 and blockage of 3.5% are used.

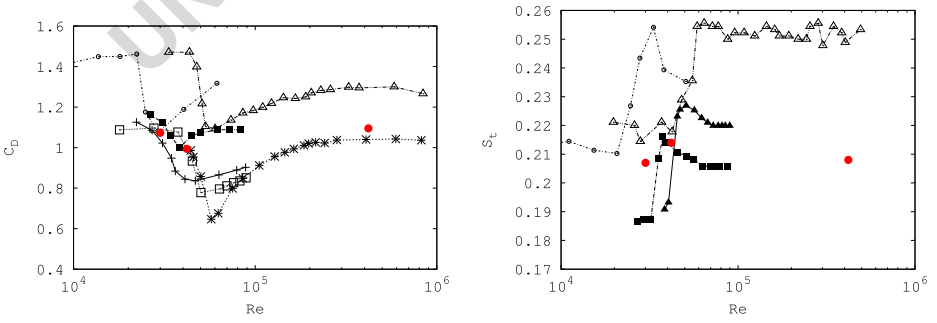

Fig. 5 **a** Drag coefficient and **b** non-dimensional vortex shedding frequency. Comparison with available results in the literature. ○ $k_s/D = 3 \times 10^{-2}$ [4], + $k_s/D = 2 \times 10^{-2}$ [15], ■ $k_s/D = 1.2 \times 10^{-2}$ [19], ✻ $k_s/D = 9 \times 10^{-3}$[13], △ $k_s/D = 9 \times 10^{-3}$ [4], □ $k_s/D = 9 \times 10^{-3}$ [15], ▲ $k_s/D = 7 \times 10^{-3}$ [19], ● present LES

JrnlID 10494_ArtID 9866_Proof#1 - 14/10/2017

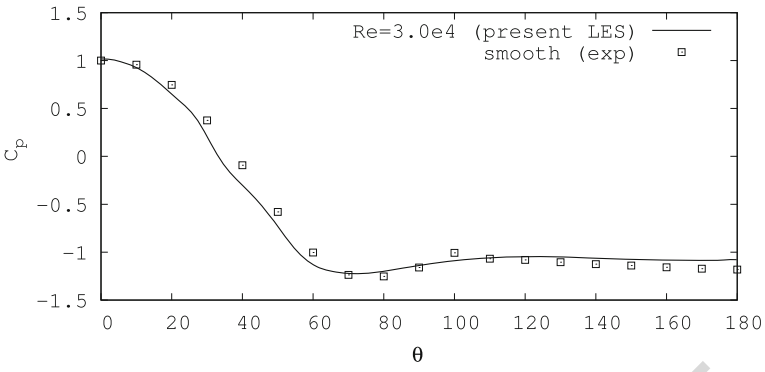

(a)

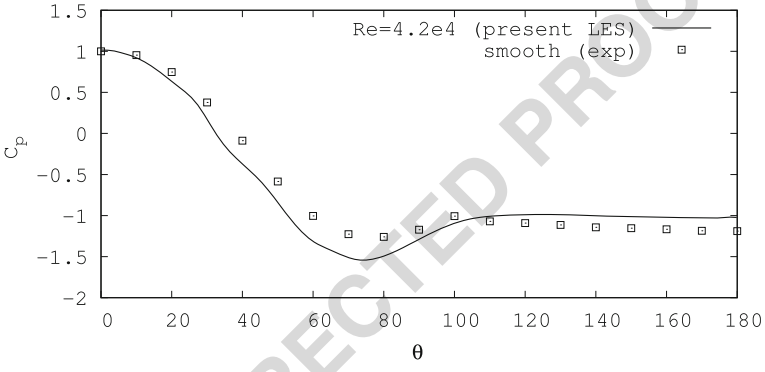

(b)

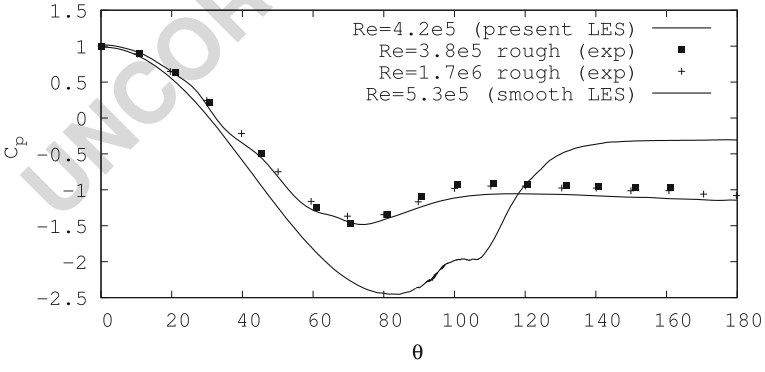

(c)

Fig. 6 Pressure coefficient distribution along the cylinder circumference. Comparison with experimental results. **a** $Re = 3 \times 10^4$; **b** $Re = 4.2 \times 10^4$; **c** $Re = 3 \times 10^5$. Experiments for the smooth cylinder are taken from [43]. Measurements for the rough cylinder from [22] at $Re = 3.8 \times 10^5$, $k/D = 1.22 \times 10^{-2}$ and [20] at $Re = 1.7 \times 10^6$, $k/D = 1.0 \times 10^{-2}$. LES for the smooth cylinder at $Re = 5.3 \times 10^5$ taken from [9]

For the rough cylinder at the high Reynolds number, the flow for this roughness height is in the transcritical regime [13]. In this regime, pressure distribution and drag coefficient have a constant behaviour independently of the Reynolds number, and only function of the roughness parameter [13, 19]. Thus, at $Re = 4.2 \times 10^5$, pressure distribution is compared with the experimental measurements of [22] at $Re = 3.8 \times 10^5$ and $k/D = 1.22 \times 10^{-2}$ and with those of [20] at $Re = 1.7 \times 10^6$ and $k/D = 1.0 \times 10^{-2}$. According to [9], for the smooth cylinder at the Reynolds number under study the flow should be in the critical regime, and flow symmetry is attained somewhere in between $Re = 3.8 \times 10^5$ and $Re = 5.3 \times 10^5$. Considering this, for comparison with the smooth cylinder, the symmetric flow conditions observed at $Re = 5.3 \times 10^5$ are used here.

For $Re = 3 \times 10^4$ (Fig. 6a), the pressure distribution almost matches that of the smooth cylinder and only small differences are observed in the base pressure, the rough cylinder being slightly less negative than the smooth one. Indeed, the average drag coefficient obtained is in agreement with that measured on smooth cylinders (see Table 3). As the Reynolds number increases, at $Re = 4.2 \times 10^4$, there is a reduction in the drag coefficient, which seems to point out the onset of the critical regime. For the roughness size under study, this decrease is about 15% compared to the smooth cylinder (see values in Table 3). Actually, for the smooth cylinder in the range of Reynolds numbers analysed, a plateau in the drag coefficient is observed up until the flow enters the critical regime at $Re \approx 2 \times 10^5$, with $C_D = 1.18$ [12]. If the pressure coefficient distribution is compared with that of the smooth cylinder(see also Fig. 6b), the pressure minimum is lower and there is a small increase in the base pressure. Contrary to the critical regime for smooth cylinders, characterised by the formation of a laminar separation bubble (LSB) with delayed final turbulent separation of the boundary layer [9, 44], there is no presence here of LSBs (a LSB can be identified as a plateau in the pressure coefficient distribution, e.g. the plateau in the pressure observed for the smooth cylinder at $\theta \approx 100°$ Fig. 6c). This is in good agreement with previous experimental studies which no LSBs are observed for relatively large values of surface roughness such as the one used in the present work [13, 19].

One of the effects of the roughness is to trigger early transition to turbulence, shifting the critical regime to lower Reynolds numbers whilst the resulting critical (minimum) drag coefficient increases as the roughness height increases [13]. Considering the flow regimes for the roughened cylinder identified by [13], for the particular cases considered here the flow at $Re = 4.2 \times 10^5$ (Fig. 6c) has already entered the transcritical regime. Indeed, there is a recovery in the drag coefficient of about 9% (see Table 3). Note that in spite of the different Reynolds numbers for the experimental measurements plotted in the figure, the pressure distributions along the cylinder are almost the same, as in the transcritical regime the flow parameters attain a nearly constant behaviour regardless of the Reynolds number and only depending on the roughness size [16]. The agreement of the numerical results obtained with experimental data is also rather good; small differences are expected as the roughness height is not the same as in the experiments. However, if the roughened cylinder is compared to the smooth one, large differences are observed. As was mentioned above, the flow for the smooth cylinder corresponds to the critical regime where the magnitude of the minimum pressure has decreased almost to a minimum value whilst the delayed separation of the boundary layer has allowed a recovery in the back pressure with the consequent decrease in the drag coefficient. For the rough cylinder, the pressure minimum is considerably larger whilst the early separation of the boundary layer has enlarged the base pressure zone in the rear end of the cylinder. As will be further discussed, these changes in the boundary layer not only introduce large changes in the forces acting on the cylinder but also in the vortex shedding and flow topology. Also note that the location of the minimum pressure moves

JrnlID 10494_ArtID 9866_Proof#1 - 14/10/2017

Table 3 Flow parameters

Re	C_D	$C_{D,rms}$	$C_{L,rms}$	St	L_r/D	$-C_{pb}$	$-C_{p,min}$	θ_{min}	θ_0
3.0×10^4	1.073	0.047	0.309	0.206	1.01	1.077	1.22	71.5	33
4.2×10^4	0.994	0.041	0.316	0.214	0.948	1.024	1.548	74.0	32.2
4.2×10^5	1.095	0.059	0.393	0.207	0.891	1.139	1.48	72.7	32.2
4.1×10^4 (smooth) [45]	1.14	–	–	0.186	0.89	–	–		
$3.0 \times 10^4 - 4.2 \times 10^4$ (smooth) [12]	1.18	–	–	–	–	–	–		
3.8×10^5 (rough) [22]	0.99	–	–	–	–	0.99	1.39	73	34
3.8×10^5 (smooth) [9]	0.481	0.061	0.217	0.238/0.358	0.641	0.48	2.46/1.77	81.3/286.5	31.6/320
5.3×10^5 (smooth) [9]	0.296	0.011	0.071	0.368	0.727	0.305	2.45	83	30.5

Comparison with literature available numerical and experimental results. C_D drag coefficient, $C_{D,rms}$ fluctuating drag, $C_{L,rms}$ fluctuating lift, St non-dimensional vortex shedding frequency, L_r/D recirculation length, $-C_{pb}$ base pressure, $-C_{p,min}$ minimum pressure coefficient, θ_{min} azimuthal location for minimum pressure coefficient, θ_0 azimuthal location for zero pressure coefficient

slightly downstream towards the cylinder apex when the drag is reduced from 1.073 to 0.994 (at $Re = 3.0 \times 10^4$ and $Re = 4.2 \times 10^4$, respectively) and then, it moves upstream, towards the front stagnation point with the further drag recovery. This behaviour is similar to the changes that occur in the smooth cylinder when the flow goes from the subcritical to the critical regime, but in this case changes are of a smaller magnitude compared to the smooth cylinder. Actually, the rather small changes in the drag coefficient seems to point out that for larger roughness height the flow would shift directly from subcritical to transcritical regime as [19] suggested.

The non-dimensional vortex shedding frequency is nearly independent of the Reynolds number (Fig. 5b and Table 3), with a value around $fD/U_{ref} \approx 0.206-0.214$. These values are quite close to those reported in the subcritical regime for smooth cylinders and comparable to those reported by [19]. However, compared to the experimental results of [4], large differences are observed, especially at $Re = 4.2 \times 10^5$. It should be stressed that at this Reynolds number there are no other experimental measurements available for rough cylinders. Yet, it is difficult to argue if these differences are due to the experimental arrangement (see discussion in Appendix A) or to numerics. Note also that at lower Reynolds number [4] results also deviate from those of [19] at comparable k_s/D values.

On the other hand, if the vortex shedding frequency for the rough cylinder at $Re = 4.2 \times 10^5$ is compared to that of the smooth cylinder at similar Reynolds numbers (see Fig. 7) there are also large differences. In Fig. 7, the time history of the drag and lift coefficients together with the energy spectrum of the lift fluctuations are plotted. Lift fluctuations ($C_{L,rms}$) are larger than the corresponding values for the smooth cylinder in this range of Reynolds number (note the change in the scale in Fig. 7c, e), whereas the vortex shedding frequency is lower for the rough cylinder. This effect is known to be related to the position of the boundary layer separation, as both vortex shedding frequency and drag coefficient are affected by this parameter [46]. For the rough cylinder at all Reynolds numbers, separation occurs before the cylinder apex (see discussion in Section 3.3), thus producing a wide wake behind the cylinder and a larger drag coefficient. In contrast, for the smooth cylinder, Reynolds numbers around $Re = 4.2 \times 10^5$ correspond to the critical regime where separation is delayed. As a consequence, the behaviour of the shear layers is altered, forming a narrow wake with a reduction of the drag coefficient [9, 10]. As suggested by [47] and later confirmed by several experimental and numerical studies [10, 48–50], a universal vortex shedding frequency ($S_t^* = S_{t,corr}(1 - C_{pb})^{-0.5} d_w/D \approx 0.164$) in terms of the wake width(d_w) can be defined for the wake behind bluff bodies. Thus, it should be expected that with the increase in the distance between both shear layers and the wake width, the non-dimensional vortex shedding frequency should decrease, as is seen for the rough cylinder. For the cases studied here, the non-dimensional vortex shedding frequency obtained are within 95% of the value predicted by the correlation $S_t^* = S_{t,corr}(1 - C_{pb})^{-0.5} d_w/D \approx 0.164$. Note that for evaluating the correlation the wake width must to be estimated. In this case, it is estimated following [51] definition, also used in [10]. According to this, the wake width is $d_w/D = 1.123,\ 1.09,\ 1.136$ for $Re = 3.0 \times 10^4,\ 4.2 \times 10^4,\ 4.2 \times 10^5$, respectively.

3.2 Overview of the instantaneous flow

In Fig. 8, the instantaneous wake structures at $Re = 4.2 \times 10^4$ are shown by means of iso-contours of the second invariant of the velocity gradient ($Q = 15$), pressure fluctuations and turbulent kinetic energy. As has been discussed in the previous section, vortex shedding does occur at all Reynolds numbers and, as can be seen from Fig. 8a, a von Kármán vortex street is formed behind the cylinder. The wake structure is quite similar for all Reynolds

JrnlID 10494_ArtID 9866_Proof#1 - 14/10/2017

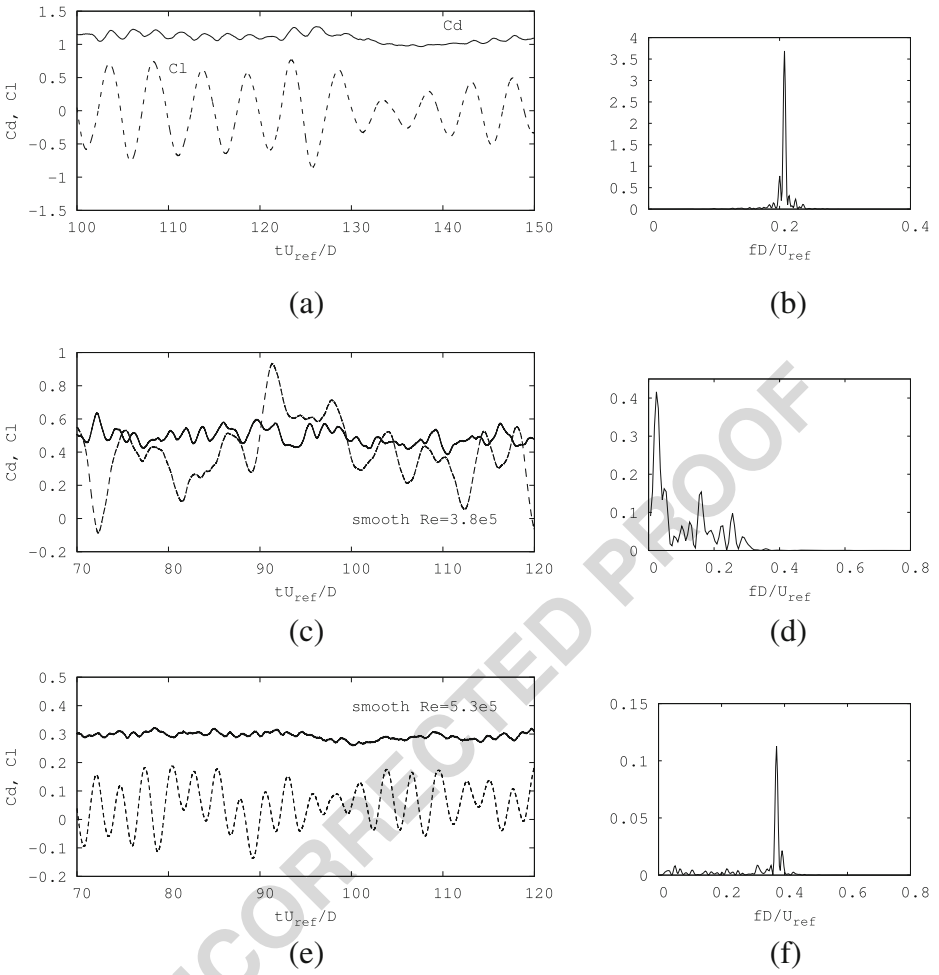

Fig. 7 Segment of the time history of (- - - - -) lift and (———) drag coefficients for the rough and smooth cylinders (left) and energy spectrum of the lift fluctuations (right). **a**, **b** $Re = 4.2 \times 10^4$ (rough cylinder), **c**, **d** $Re = 3.8 \times 10^4$ (smooth cylinder), **e**, **f** $Re = 5.3 \times 10^5$ (smooth cylinder). Results for the smooth cylinder are from [10]

numbers and resembles that formed behind a smooth cylinder in the subcritical regime, with large stream-wise vortices connecting the two-dimensional vortex tubes. However, contrary to the subcritical smooth cylinder, significant pressure fluctuations along the cylinder can be observed (see Fig. 8b). These fluctuations are triggered on top of the surface roughness elements and indicate a certain level of turbulent kinetic energy along the cylinder boundary layer, as can also be observed in Fig. 8c, close to the cylinder shoulder. Indeed, these fluctuations on top of the roughness elements are responsible of rapidly triggering the transition to turbulence once the boundary layer is detached from the cylinder, as can be ~~see~~ from the figure.

A close inspection of the separated shear layer and cylinder near-wake is shown in Fig. 9. In the figure, instantaneous span-wise vorticity isocontours ($\omega_z = \pm 15$) are used to visualise

JrnlID 10494_ArtID 9866_Proof#1 - 14/10/2017

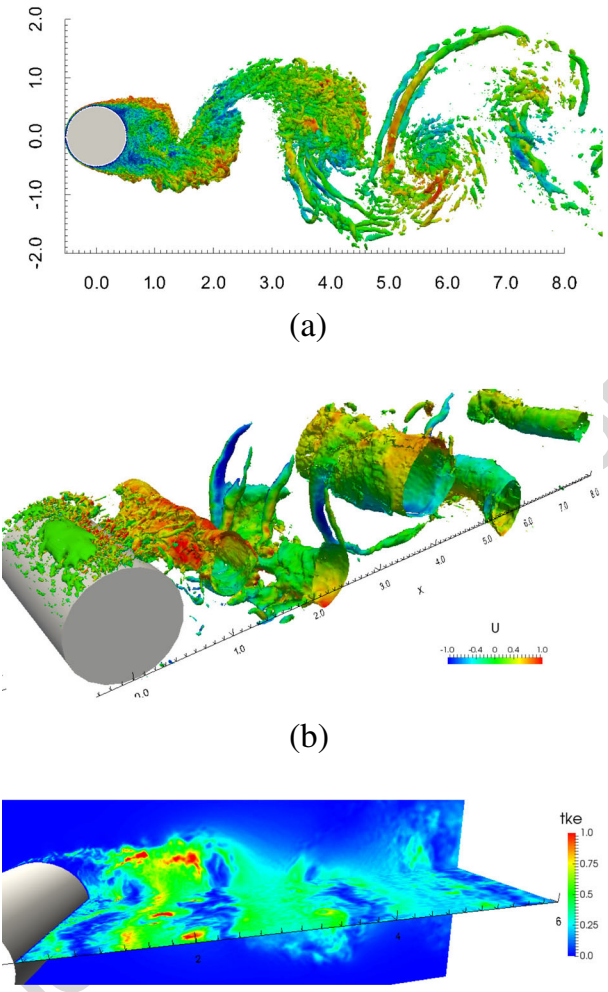

Q3

Fig. 8 Instantaneous flow structures at $Re = 4.2 \times 10^4$. **a** Q-isosurfaces $Q = 15$; and **b** pressure fluctuation isosurfaces $p'/\rho\, U_{ref}^2 = -0.2$ coloured by stream-wise velocity; **c** turbulent kinetic energy

the structures in the boundary layer. The inception of small-scale fluctuations, even at the subcritical Reynolds number of $Re = 3.0 \times 10^4$, is observed close to the cylinder apex (for reference in the figure, the angular position at 90° is marked with a line). This is in contrast with the smooth cylinder in which the flow separates laminarly and these small scale fluctuations are triggered in the separated shear-layer in this regime (subcritical regime). Although not visible in Fig. 9a, b, these boundary layer instabilities are triggered quite early (see also Fig. 10). In Fig. 10, the time history and spectrum of the stream-wise velocity fluctuations of three different numerical probes at $(r, \theta) \equiv (0.54D, \theta)$ being $\theta = 45°,\ 70°$ and$90°$ for $Re = 4.2 \times 10^4$ and $Re = 4.2 \times 10^5$ are plotted. At 45° from the front stagnation point, the fluctuations in the boundary layer are barely noticeably for $Re = 4.2 \times 10^4$. Actually, they appear as very small fluctuations on top of the periodic behaviour of the velocity due to vortex shedding (see Fig. 10a). However, as the boundary layer evolves, fluctuations are

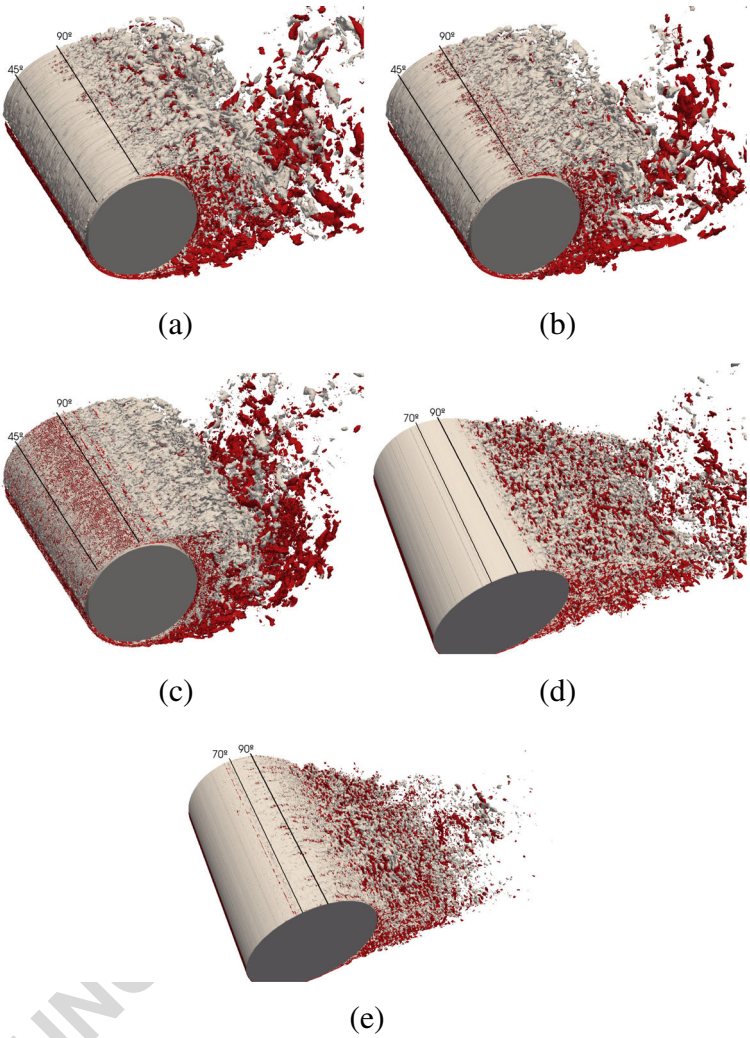

Fig. 9 Instantaneous span-wise vortical structures. $\omega_z = \pm 15$. **a** $Re = 3 \times 10^4$; **b** $Re = 4.2 \times 10^4$; **c** $Re = 4.2 \times 10^5$; **d** $Re = 3.8 \times 10^5$ (smooth cylinder) and **e** $Re = 5.3 \times 10^5$ (smooth cylinder)

amplified and at $\theta = 70°$ become more significant. The inception of these fluctuations on top of the regular variation of the ~~velocity,~~ can also be seen in the energy spectrum (see Fig. 10c). In the figure, apart from the vortex shedding peak (f_{vs}), there is a broad-band peak at a larger frequency (marked in the figure as f_{BL}). This peak ~~disappear~~ in the background of the fluctuations at $\theta = 90°$ once the boundary layer is detached from the cylinder surface. It seems, however, that these instabilities occur at a sublayer scale for the two lower Reynolds numbers (the numerical probes are located at a radial distance of $r/D = 0.54$) and they barely affect the boundary layer as can be seen in Fig. 9a,b at these locations. This is in agreement with [13], who observed that in the subcritical regime the boundary layer was laminar up to the separation point.

JrnlID 10494_ArtID 9866_Proof#1 - 14/10/2017

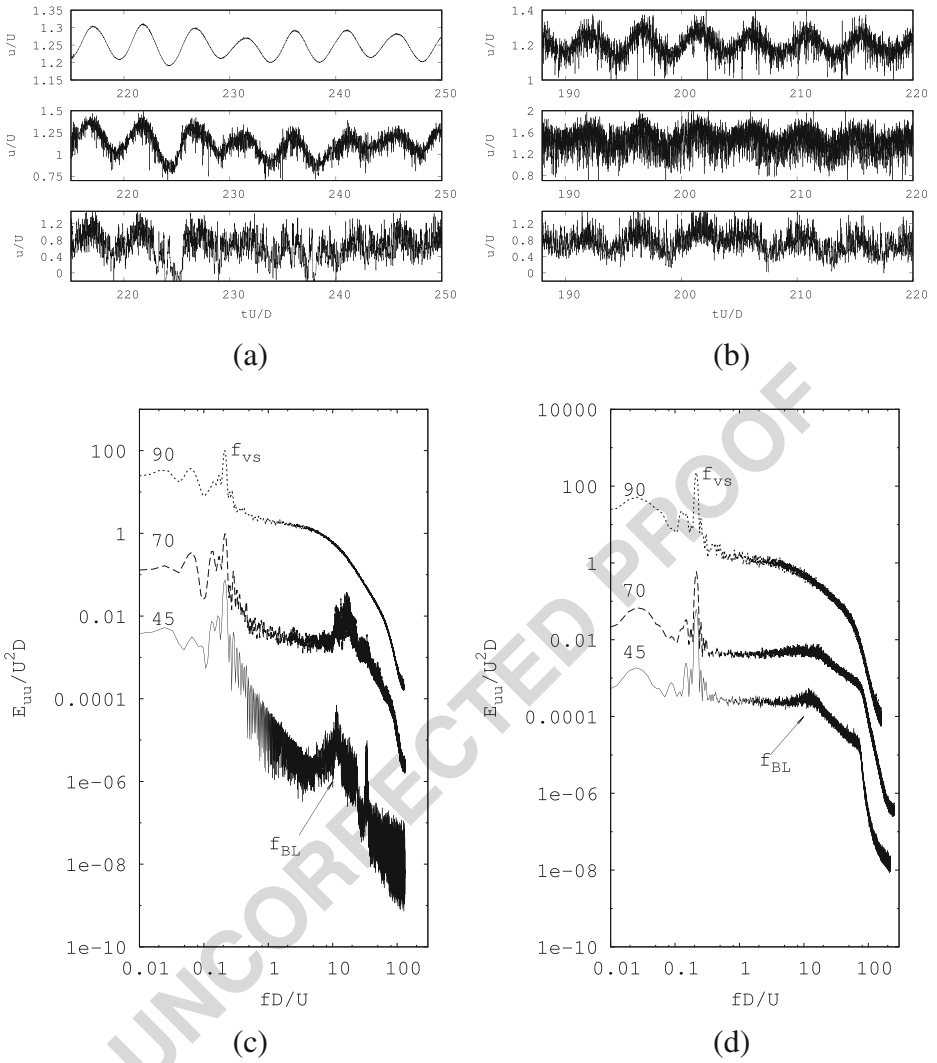

Q4 **Fig. 10** Time history and power spectrum of the stream-wise velocity fluctuations in the boundary layer at 45°, 70° and 90° from the front stagnation point. For Reynolds numbers **a**, **c** $Re = 4.2 \times 10^4$, **b**, **d** $Re = 4.2 \times 10^5$

At $Re = 4.2 \times 10^5$, the boundary layer is in transition as early as at $\theta = 45°$ and small-scale fluctuations can be seen throughout the whole boundary layer (Fig. 9c). If compared to the smooth cylinder at $Re = 3.8 \times 10^5$ and $Re = 5.3 \times 10^5$ (Fig. 9d,e), it is possible to observe the changes roughness introduces in the boundary layer. The magnitude of the fluctuations are larger than those observed at the lower Reynolds numbers (see Fig. 10b). Also note the change in shape of the energy spectrum at this Reynolds number and how the peak of the boundary layer instabilities is almost embedded into the background fluctuations. At the cylinder shoulder (i.e. $\theta = 90°$), as for the lower Reynolds numbers, the flow is already detached and turbulent shear-layers can be observed departing from that location.

JrnlID 10494_ArtID 9866_Proof#1 - 14/10/2017

After separation, the wake is more similar to the one observed for the rough cylinder at $Re = 4.2 \times 10^4$ (see Fig. 8a), than the wake of smooth cylinders at comparable Reynolds numbers. For the smooth cylinder boundary layer instabilities are triggered near the cylinder apex, but transition to turbulence occurs just after separation [9, 10] (see Fig. 9d,e) giving place to a narrow wake. The fact that surface roughness triggers flow fluctuations early forces the rapid separation, thus changing the topology of the near wake as it is shown in the next section.

As mentioned earlier, the broad-band peak observed (marked in the figures as f_{BL}), is more evident for the two lower Reynolds numbers, i.e. $Re = 3 \times 10^4$ and $Re = 4.2 \times 10^4$. In Fig. 11, a comparison of the spectrum at $\theta = 70°$ for the three Reynolds numbers is plotted. The location of this peak does not seem to vary with Reynolds number, being around $f\ D/U_{ref} = 12.1$ for all cases. A priori, one might think that this frequency, which seems to be associated with the instabilities of the boundary layer, should vary with the Reynolds number as the frequency of the instabilities in the shear layer does ($f_{SL}/f_{vs} = 0.0235 Re^{0.67}$, [52]). However, as instabilities are here triggered by the surface roughness and not by a convective-type mechanism as in the smooth cylinder in the subcritical regime

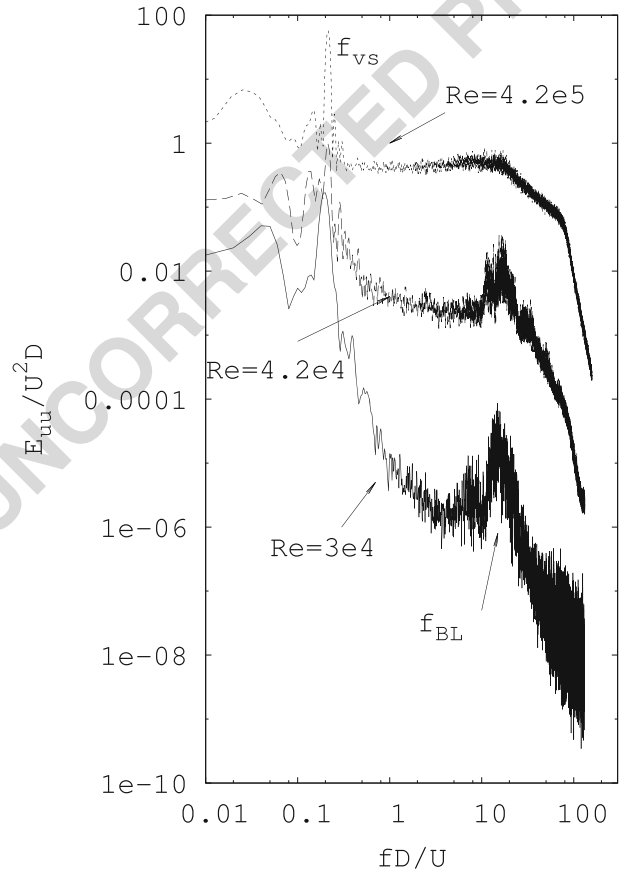

Fig. 11 Energy spectra of the stream-wise velocity fluctuations at $\theta = 70°$ for the different Reynolds numbers studied

JrnlID 10494_ArtID 9866_Proof#1 - 14/10/2017

[53], then this peak may be also associated with the surface roughness size. Note that if the frequency of this peak is defined in terms of the roughness height, it corresponds with a non-dimensional frequency centred at $fk/U_{ref} = 0.242$. The value of this frequency is close to the values measured on mounted circular cylinders and hemispheres $fk/U_{ref} \approx 0.222 - 0.225$ by [54] and on mounted spheres $fk/U_{ref} \approx 0.204$ by [55]. Nonetheless, as no parametric studies regarding the roughness size are conducted in the present work, no conclusions can be derived on the influence of the roughness size with the boundary layer instability frequency.

3.3 Boundary-layer and wake statistics

Tangential velocity profiles along the boundary layer in the vicinity of flow separation for all Reynolds numbers are plotted in Fig. 12. Velocity profiles are almost the same for the three Reynolds numbers, but as the flow approaches separation near the cylinder apex, the boundary layer for the lower Reynolds number becomes thicker. Flow separation occurs close to the cylinder apex at all Reynolds numbers. However, here the location of the separation point is not determined by the position where the wall stress becomes zero. As observed by [56], for a rough surface the wall stress becomes zero because of flow reversal inside the roughness sublayer rather than with separation of the flow from the surface. Moreover, they found that actual flow separation is related with the location where the total stress becomes negative at the roughness crest. Following [56], we have defined the location where flow reversal starts θ_r, as the angular position where $\tau_w = \mu \partial u_\theta / \partial n$ becomes zero and, the location of flow separation θ_{sep} as the angular position where the total stress at the roughness crest becomes negative. The total stress is defined as

$$\tau_{crest} = \left(\mu \frac{\partial u_\theta}{\partial n} + \rho \left\langle u_r' u_\theta' \right\rangle \right)_{k_{crest}} \tag{6}$$

In the above equation, μ accounts for both the fluid and the subgrid scale viscosity. For the rough cylinder, it has been found that flow reversal starts as early as $\theta_r \approx 78°$, whereas separation at all Reynolds numbers occurs close the cylinder apex at $\theta_r \approx 85.5-88°$, similar to the values reported for the smooth cylinder in the sub-critical regime. These locations are reported in Table 4. As can be seen, although roughness affects the location where transition to turbulence takes place, the separation of the boundary layer for the two lower Reynolds numbers remains almost the same as for the smooth cylinder. However for $Re = 4.2 \times 10^5$,

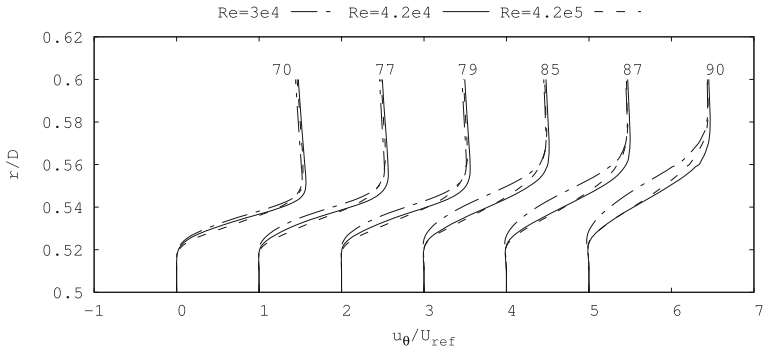

Fig. 12 Tangential velocity profiles (u_θ / U_{ref}) along the boundary layer

Table 4 Angular positions for flow reversal θ_r and flow separation θ_{sep} in the boundary layer

Re	θ_r	θ_{sep}
3.0×10^4	78	88
4.2×10^4	78	87.5
4.2×10^5	77	85.5
3900 (smooth sub-critical) [38]	–	88
3.8×10^5 (smooth critical) [9]	–	145/219
5.3×10^5 (smooth critical) [9]	–	148

Comparison with the smooth cylinder at sub-critical and critical Reynolds numbers

separation is triggered early thus affecting the topology of the near wake as will be discussed later. The value of the total stress at the roughness crest has been also used to determine whether the flow in the boundary layer is in the transitional or fully rough regime. Although in the case of the cylinder the shear stress at the roughness crest varies with the angular position, when it attains its maximum value (close to the angular position of 70°) the value of $k^+ = k\,u_\tau/\nu \approx 60$ for $Re = 3.0 \times 10^4$ (with $u_\tau = \sqrt{\tau_{crest}/\rho}$). This value increases up to $k^+ \approx 1870$ for the highest Reynolds number. Thus, given these values it might be stated that for the lowest Reynolds number the flow in the boundary layer is in the transitional rough regime, whereas at the high Reynolds number it is fully rough for most of the forward part of the cylinder.

In Fig. 13, the boundary-layer integral quantities for the rough case at $Re = 4.2 \times 10^5$ are compared with the experimental data by [16] at $Re = 3 \times 10^5$, but for smaller roughness ($k/D = 2.66 \times 10^{-3}$) and with the smooth-cylinder data at $Re = 3.8 \times 10^5$ [9]. Here, δ_{95} is the location where the velocity is 95% of the velocity outside the boundary layer, δ_1 and δ_2 are the displacement and momentum boundary-layer thicknesses, respectively defined as:

$$\delta_1 = \int_0^{\delta_{95}} \left(1 - \frac{U}{U_e}\right) dy; \quad \delta_2 = \int_0^{\delta_{95}} \frac{U}{U_e}\left(1 - \frac{U}{U_e}\right) dy. \tag{7}$$

The expected trends can be observed: roughness increases all these quantities; they also increase along the cylinder surface, especially near separation.

Velocity profiles at selected locations along the boundary layer are shown in Fig. 14. Comparison between the same three datasets are carried out. The near-wall behaviour of the experimental data (the filled triangles, digitised from Fig. 3b in [16]) is anomalous: the velocity does not appear to approach $U/U_e = 0$, but rather $U/U_e = 0.2$. This behaviour is particularly noticeable in the measurements at $\theta = 98°$: the flow here is separated, and negative velocities should be expected near the wall; the experimental profile has the expected shape, with a reversed concavity, but the velocity remains positive. We conjecture that the anomalous behaviour is not caused by experimental error (which would have to be of the order of 20%), but rather by a mislabelling of the axis. Therefore, we report both the raw data digitised from the figure, and the one corrected according to our conjecture (the filled circles).

Compared to the smooth-wall case, a significant momentum deficit is observed in the rough-wall cylinders. This momentum deficit is responsible for the early separation of the flow. Slightly negative velocities (due to the flow separation behind the roughness elements) are observed below the crest. The agreement with the (corrected) experimental data is remarkable, given the difference in roughness height between the two cases. This may be

JrnlID 10494_ArtID 9866_Proof#1 - 14/10/2017

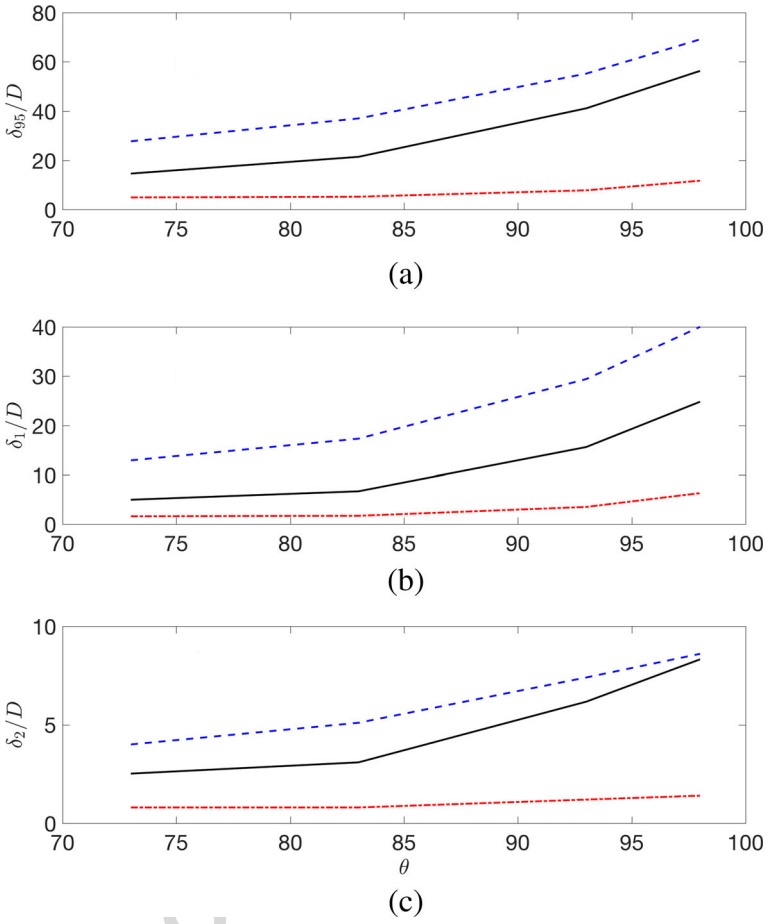

Fig. 13 Integral boundary layer quantities. Dashed-dot: Smooth cylinder (data from simulations from [9]); solid: rough cylinder, experimental data by [16]; dashed: present calculation, $Re = 4.2 \times 10^5$. **a** Boundary layer thickness; **b** displacement thickness; **c** momentum thickness

related to Townsend's outer-layer similarity hypothesis [57], and is an issue that deserves further study.

Near-wake mean-field visualisations can provide further evidence of how roughness affects the flow behaviour. Figures 15 and 16 show the structure of the near wake in terms of time-averaged first- and second-order statistics for $Re = 4.2 \times 10^5$. For comparison with the critical wake for the smooth cylinder, the same patterns are shown at $Re = 5.3 \times 10^5$. For the smooth cylinder in the onset of the critical regime, the flow is asymmetric and symmetry is recovered at the end of the critical regime [9]. Statistics are shown here at $Re = 5.3 \times 10^5$, once the flow has recovered its symmetry (see [9] for details). Even though the flow past the rough cylinder is at different regimes, i.e., subcritical at $Re = 3.0 \times 10^4$, critical at $Re = 4.2 \times 10^4$ and transcritical at $Re = 4.2 \times 10^5$, for the surface roughness heigh in this study, differences in the separation point are not large enough to change the wake topology behind the cylinder, which remains almost the same regardless of the Reynolds number. For this reason in Figs. 15 and 16 only the wake for $Re = 4.2 \times 10^5$ is shown.

JrnlID 10494_ArtID 9866_Proof#1 - 14/10/2017

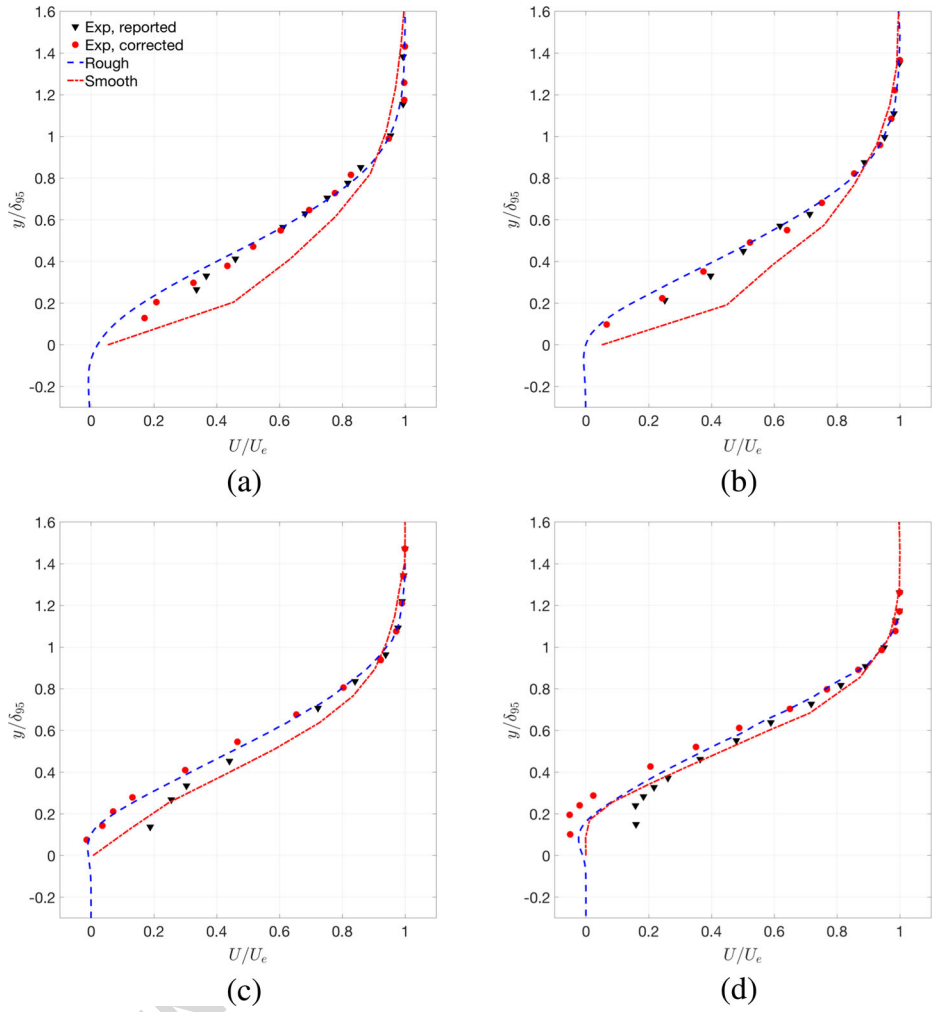

Fig. 14 Mean velocity profiles. Dashed-dot: Smooth cylinder [9]; triangle: rough cylinder, experimental data by [16]; circle: corrected experimental data; dashed: present calculation, $Re = 4.2 \times 10^5$. **a** $\theta = 73°$; **b** $\theta = 83°$; **c** $\theta = 93°$; **d** $\theta = 98°$. y is the radial distance measured from the roughness crest

The overall shape of the near wake, especially the first-order statistics, resembles the wake of the smooth cylinder in the subcritical regime (see for instance figures 4-9 of [58] at $Re = 1.0 \times 10^4$ or figures 6 and 8 in [45] at $Re = 4.13 \times 10^4$). In Fig. 15, contour plots of the stream-wise velocity, span-wise vorticity and pressure coefficient are shown for the near wake. The minimum velocity deficit in the wake centreline is $\langle u \rangle / U_{ref} = -0.265$, slightly smaller than for $Re = 3 \times 10^4$ and $Re = 4.2 \times 10^4$ (see Table 5). These values are quite close to those of the smooth cylinder. Nonetheless, the overall wake topology at $Re = 4.2 \times 10^5$ is quite different when compared to the smooth cylinder at $Re = 5.3 \times 10^5$. The wake is much wider than that of the critical smooth cylinder. As mentioned in the previous section, roughness triggers early transition to turbulence and boundary layer separation. Thus, turbulent shear layers depart almost parallel to each other, similar to the way laminar

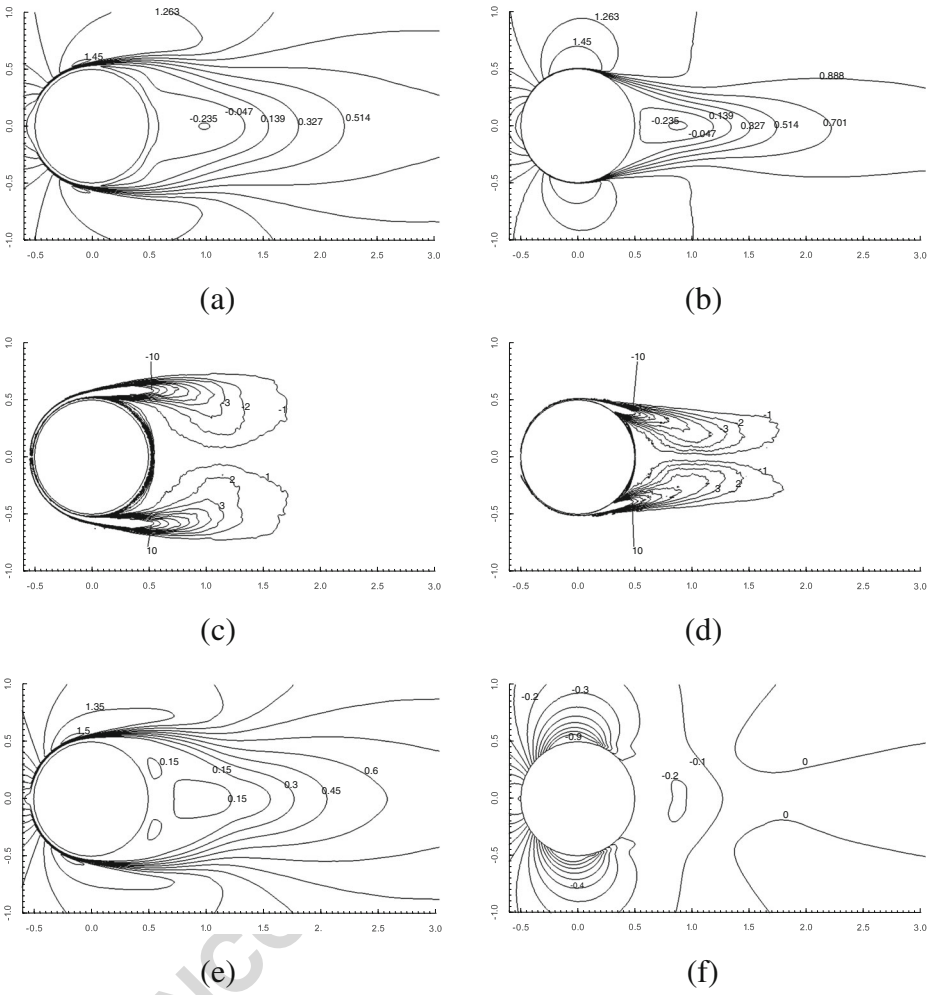

Fig. 15 Transcritical wake topology at $Re = 4.2 \times 10^5$. Comparison with the smooth cylinder at $Re = 5.3 \times 10^5$. First order statistics: **a**, **b** stream-wise velocity; **c**, **d** span-wise vorticity; (e,f) pressure coefficient

shear layers separate from the cylinder in the subcritical regime (see Fig. 15c). Due to this early separation, the wake is wider than that of the smooth cylinder. For the critical smooth cylinder, shear layers are bent towards the wake centreline (see Fig. 15d) changing the way vortices are shed into the wake and the topology of the vortex formation region, as reported in [9] and [10]. Stream-wise velocity iso-contours are also different, with the cross-stream separation between velocity maxima in the wake larger for the rough cylinder in comparison with the smooth critical cylinder (see Fig. 15a). Moreover, pressure patterns are completely different, pressure levels being higher, and the minimum occurs in the front face of the cylinder, approximately at 70° (see also the comparison in Fig. 6c), whereas for the critical smooth cylinder pressure reaches a minimum near the cylinder shoulder with a higher base pressure.

JrnlID 10494_ArtID 9866_Proof#1 - 14/10/2017

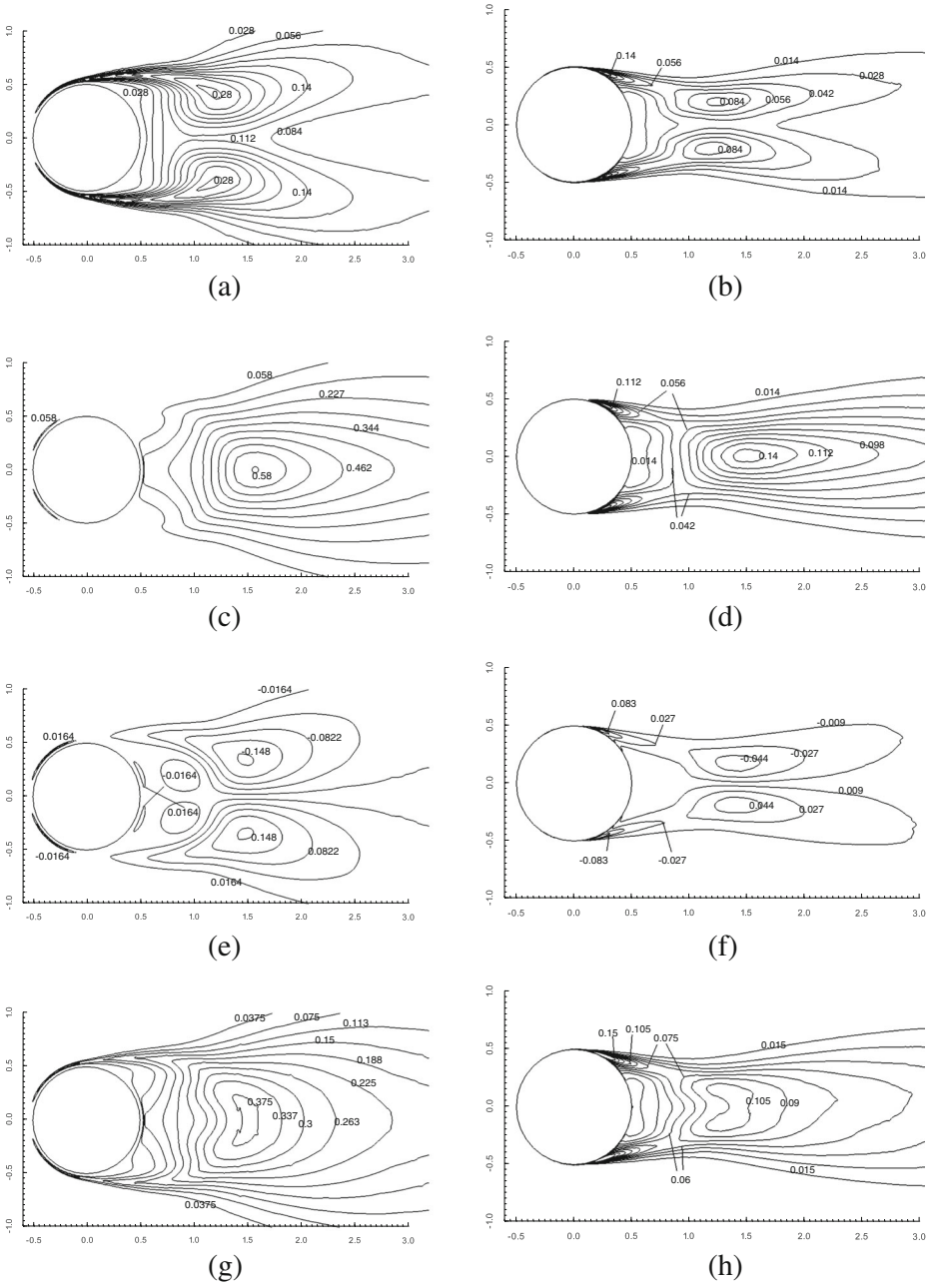

Fig. 16 For caption see facing page. Transcritical wake topology at $Re = 4.2 \times 10^5$. Comparison with the smooth cylinder at $Re = 5.3 \times 10^5$. Second order statistics: **a**, **b** stream-wise normal Reynolds stresses; **c**, **d** cross-streamwise normal Reynolds stresses; **e**, **f** shear Reynolds stresses; **g**, **h** turbulent kinetic energy

JmlID 10494_ArtID 9866_Proof#1 - 14/10/2017

Table 5 Minimum velocity deficit and maximum values of the Reynolds stresses and turbulent kinetic energy (tke) in the near wake

	3.0×10^4	4.2×10^4	4.2×10^5	$3900^{\dagger}$	$5.3 \times 10^{5\,\S}$
$\langle u \rangle_{min} / U_{ref}$	−0.313	−0.293	−0.265	−0.261	−0.253
$(x/D,\ y/D)$	(1.023, 0)	(1.013,0)	(0.981,0)	(1.396,0)	(0.885,0)
$\langle u'u' \rangle_{max} / U_{ref}^2$	0.25	0.251	0.297	0.237	0.093
$(x/D,\ y/D)$	(1.322,±0.414)	(1.266,±0.42	(1.053,±0.474)	(1.576,±0.310)	(1.124,±0.227)
$\langle v'v' \rangle_{max} / U_{ref}^2$	0.51	0.512	0.583	0.468	0.143
$(x/D,\ y/D)$	(1.655,0)	(1.543,0)	(1.562,0)	(2.00,0)	(1.494,0)
$\langle u'v' \rangle_{min} / U_{ref}^2$	−0.135	−0.139	−0.153	−0.125	−0.053
$(x/D,\ y/D)$	(1.573,±0.355)	(1.543,±0.335)	(1.446,±0.378)	(1.941,±0.391))	(1.447,±0.192)
$\langle tke \rangle_{max} / U_{ref}^2$	0.345	0.343	0.385	0.335	0.114
$(x/D,\ y/D)$	(1.459,±0.222)	(1.459,±0.222)	(1.409,±0.103)	(1.775,±0.216)	(1.291,± 0.155)

Comparison with the smooth cylinder at subcritical and critical regimes. The location of these quantities is also given. Data for $Re = 3900^{\dagger}$ (subcritical) is taken from [38] and for $5.3 \times 10^{5\,\S}$ (critical) from the authors simulations [9, 10]

JrnlID 10494_ArtID 9866_Proof#1 - 14/10/2017

Although first order statistics are similar to those in the subcritical regime, second-order statistics patterns are rather different for the rough cylinder. Reynolds stresses peaks, together with their location, for all Reynolds numbers, are also given in Table 5. For comparison, these quantities for the subcritical and critical smooth cylinders are also included. Note that the peak values for the rough cylinder are the largest, as will be discussed hereafter. It is well known that, for the smooth cylinder, the topology and peaks for the Reynolds stresses remain almost the same throughout the whole subcritical regime (see also values reported in [59] at $Re = 1.1 \times 10^5$). However, although the topology of the near wake for the rough cylinder is almost the same for the three Reynolds numbers studied, the peak values for $Re = 4.2 \times 10^5$ are consistently higher than those observed at the two lower Reynolds numbers (about 10% larger). These magnitudes, with the exception of the normal stream-wise Reynolds stresses peak, are attained just after the closure of the recirculation bubble (see Table 5). Moreover, a noticeable difference with the smooth cylinder in both the sub-critical and critical regimes is the larger magnitude of the Reynolds stresses, about 20% higher than the subcritical regime and more than 300% if compared to the critical regime. The latter effect is expected as an important part of the Reynolds stresses comes from the coherent component contribution [59, 60], which is reduced in the critical regime due to the narrowing of the wake; the wider the wake the larger the contribution of the coherent component to the Reynolds stresses.

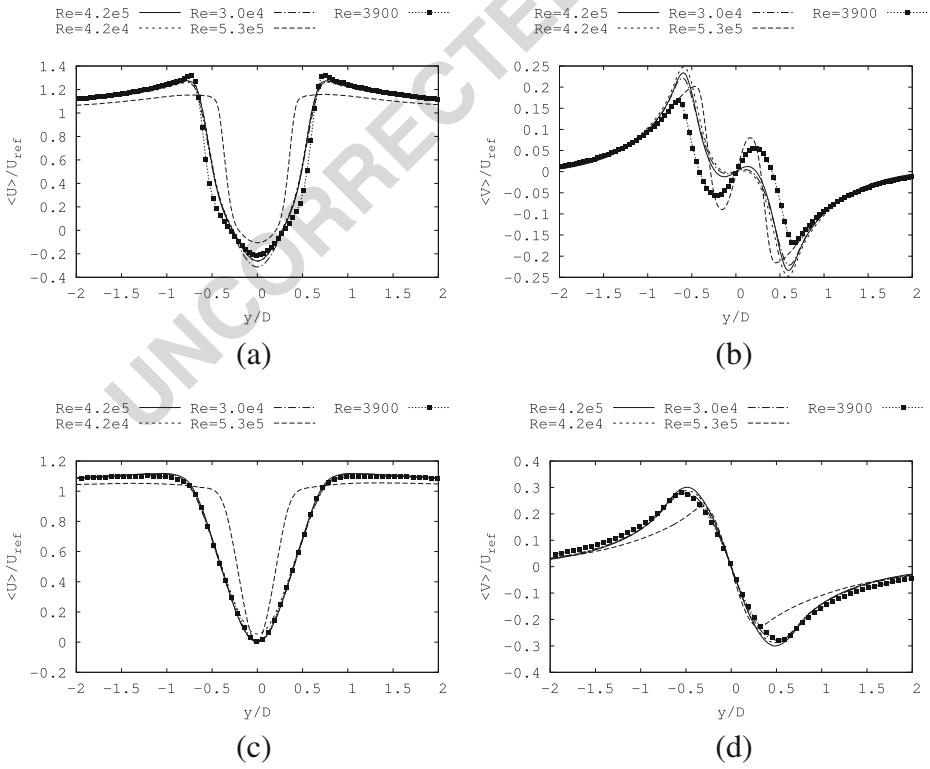

Fig. 17 First order statistics in the recirculation region behind the cylinder. **a**, **c** Stream-wise velocity and **b**, **d** cross-streamwise velocity at $\hat{x}/L_r = 0.5$ and 1

JrnlID 10494_ArtID 9866_Proof#1 - 14/10/2017

As previously mentioned, fluctuations are triggered early in the boundary layer at all Reynolds numbers. These fluctuations are visible in the averaged field in the front side of the cylinder; fluctuations follow the cylinder surface curvature (see Fig. 16). This is in contrast with the smooth cylinder in the subcritical regime where fluctuations are triggered in the detached shear-layer (see for instance [58, 61]) or for the critical just after separation (see Fig. 16b, d, f, h). Although Reynolds stresses maxima are of the same order for all Reynolds numbers, the loci of the maxima and velocity minimum are changed as these locations depend on the length of the vortex formation zone which changes with the Reynolds number (it decreases as the flow for the rough cylinder moves from the subcritical to the transcritical regime, see Tables 2 and 5).

A detailed comparison between the different Reynolds numbers is shown in Figs. 17, 18 and 19, where the near-wake statistics in the recirculation zone at selected locations are given. As the length of the recirculation region behind the cylinder (the distance from the cylinder rear end to the stream-wise location in the wake centreline where the stream-wise velocity is zero, see Table 3) changes depending on the Reynolds number, to make comparable the flow statistics in the near wake they are plotted at stream-wise locations normalised by the length of the recirculation zone, $\hat{x}/L_r$, with $\hat{x} = x - 0.5D$. In the figures, statistics are plotted at $\hat{x}/L_r = 0.5$ and 1. Moreover, the statistics for the smooth cylinder at $Re = 3900$ (subcritical regime, [38]) and for the critical regime at $Re = 5.3 \times 10^5$ are also shown in the figures. Direct comparison of the wake statistics with the smooth cylinder at $Re = 3.8 \times 10^5$

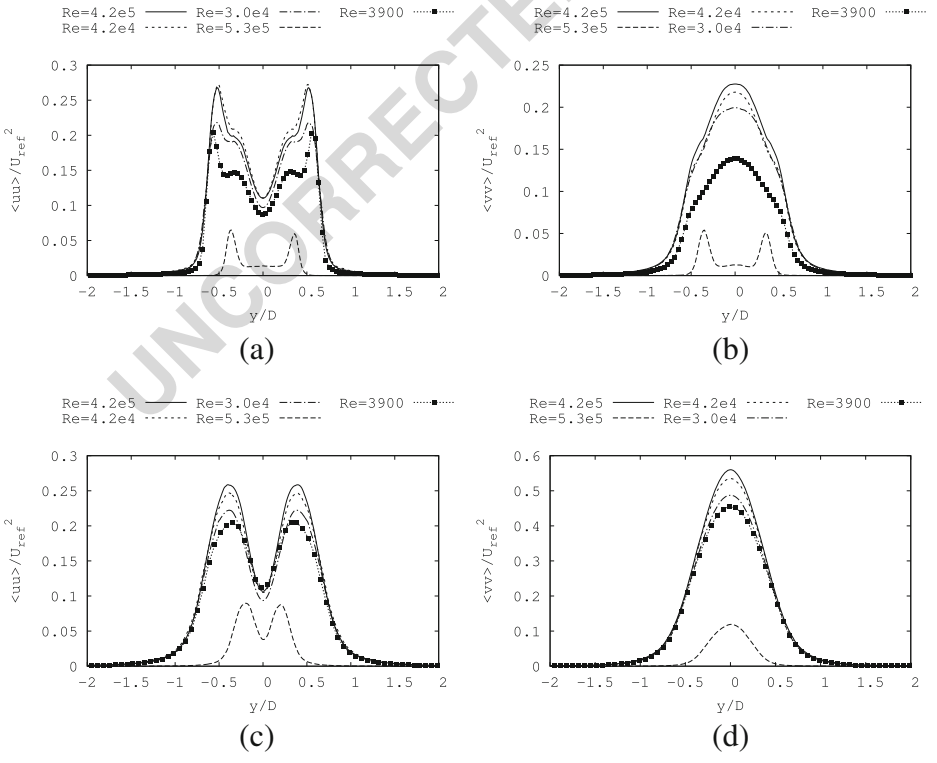

Fig. 18 Second order statistics in the recirculation region behind the cylinder. **a**, **c** Stream-wise normal and **b**, **d** cross-streamwise normal Reynolds stresses at $\hat{x}/L_r = 0.5$ and $\hat{x}/L_r = 1$

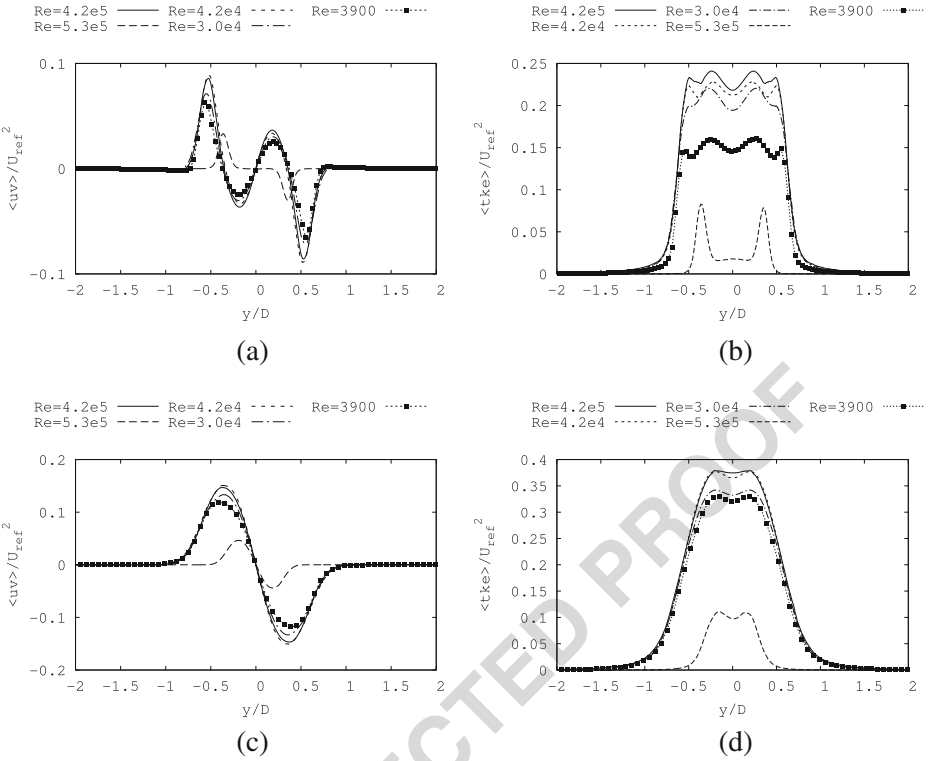

Fig. 19 Second order statistics in the recirculation region behind the cylinder. **a**, **c** Shear stresses and **b**, **d** turbulent kinetic energy at $\hat{x}/L_r = 0.5$ and $\hat{x}/L_r = 1$

are not included as at this Reynolds number the wake configuration is asymmetric due to the changes occurring in the critical regime (see [9] for more details).

First order statistics in the recirculation zone ($\hat{x}/L_r \leq 1$) compare well with the statistics for the smooth cylinder in the subcritical regime ($Re = 3900$, see Fig. 17). The topology of the near wake inside the recirculation zone depends on the position of the shear layers and on the location where the recirculation bubble closes. At the same time, the average location of the shear layers only depends on the separation point from the cylinder surface (see values reported in Table 4). This is the reason why the topology of the recirculation zone for the rough cylinder resembles that of the smooth cylinder in the subcritical regime. Note that for $\hat{x}/L_r = 0.5$ and $\hat{x}/L_r = 1$ stream-wise velocity profiles for the rough cylinder and for the subcritical smooth cylinder at $Re = 3900$ are nearly the same. As commented previously, in both cases the separation of the boundary layer occurs before the cylinder apex.

Regarding the second order statistics (see Figs. 18 and 19), as mentioned previously, for the roughened cylinder the Reynolds stresses are higher than those obtained for the smooth one. Note that stresses for the critical smooth cylinder ($Re = 5.3 \times 10^5$) are the lowest ones and, due to the narrower wake, are confined to a reduced zone close to the cylinder centreline. This is more relevant when the stresses of the rough cylinder at $Re = 4.2 \times 10^4$ are compared to those for the smooth cylinder at $Re = 5.3 \times 10^5$. The shape, magnitude and location of the peaks are completely different implying an important topology change due to the surface roughness.

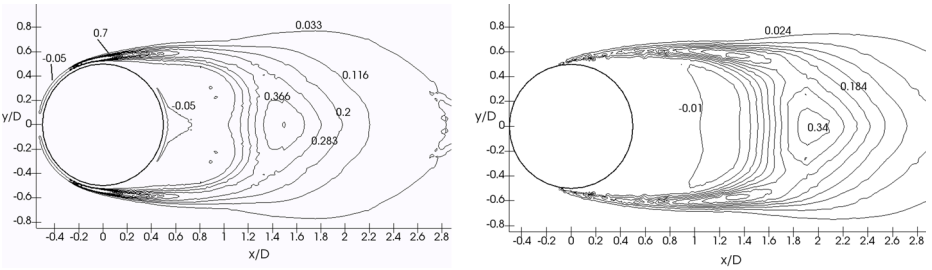

(a) (b)

Fig. 20 Contours of the production of the turbulent kinetic field. **a** at $Re = 4.2 \times 10^5$ (rough cylinder) **b** at $Re = 3900^{\dagger}$ (subcritical smooth cylinder). † Data taken from author's DNS [38]

Further insight into the distribution of the turbulent intensities can be obtained if the production of the turbulent kinetic energy (TKE) is analysed. The production of turbulent kinetic energy is

$$P_k = -\left[\overline{u_1' u_1'}\frac{\partial \overline{u}_1}{\partial x_1} + \overline{u_2' u_2'}\frac{\partial \overline{u}_2}{\partial x_2} + \overline{u_1' u_2'}\left(\frac{\partial \overline{u}_1}{\partial x_2} + \frac{\partial \overline{u}_2}{\partial x_1}\right)\right] \tag{8}$$

As the overall topology of the wake for the rough cylinder is quite similar to the smooth subcritical cylinder, in Fig. 20, contours of the production of the turbulent kinetic energy at $Re = 4.2 \times 10^5$ are compared to the smooth cylinders at $Re = 3900$. As can be seen in the figure, levels of TKE production in the wake are comparable in both cases, with peaks equal to 0.366 and 0.34, respectively. However, a region of TKE production can be observed on top of the roughness surface with an overall maximum on the cylinder shoulders and in the separated boundary layers. That is, part of the fluctuations observed in the near wake for the rough cylinder comes from the production of turbulent kinetic energy in the roughness sublayer and turbulent shear layers. This turbulent kinetic energy is convected downstream to feed the wake. This might be the reason why normal and shear stresses peaks for the rough cylinder are about 20% larger than those for the smooth cylinder in the subcritical regime (see also Table 5).

4 Concluding Remarks

Large-eddy simulations of the flow past a rough cylinder at Reynolds number of $Re = 3.0 \times 10^4$, $Re = 4.2 \times 10^4$ and $Re = 4.2 \times 10^5$ and an equivalent sandgrain roughness of height $k = 0.02D$ have been performed. An immersed boundary method has been used to enforce the no-slip condition on the rough surface. Significant changes in the boundary layer and the flow topology behind the cylinder have been observed, especially for the transcritical Reynolds number $Re = 4.2 \times 10^5$, as a consequence of the roughness elements.

Roughness introduces velocity fluctuations in the boundary layer, which are observed along the whole span of the cylinder. These fluctuations can be seen as a broadband peak in the spectrum centred about $fD/U_{ref} = 12.1$, at all Reynolds numbers. Transition to turbulence in the boundary layer is triggered as early as 45° from the cylinder front stagnation point for the higher Reynolds number, and around 70° for the lower Reynolds numbers. Boundary layer separation occurs before the flow reaches the cylinder apex as it does for the smooth sub-critical cylinder. However, at $Re = 4.2 \times 10^5$, the flow separates early as the

JrnlID 10494_ArtID 9866_Proof#1 - 14/10/2017

rough wall boundary layer has less momentum near the wall. As a consequence, the drag coefficient increases with respect to the smooth cylinder at comparable Reynolds numbers.

The wake characteristics are determined more by the location of the separation rather than by the state of the boundary layer. The wake topology resembles that of the smooth subcritical cylinder at all Reynolds numbers. At the largest Reynolds number, i.e. at $Re = 4.2 \times 10^5$, the flow would be expected to be in the critical regime, but as roughness affects the detachment of the boundary layer, the wake is much wider than that of the critical smooth cylinder. Compared to this, Reynolds stresses are higher and turbulent fluctuations are observed along the boundary layer. This increase in the fluctuations might be attributed to a higher turbulent kinetic energy production in both the boundary layer and separated shear layers. This turbulent kinetic energy is then convected downstream to the wake behind the cylinder.

Further research is needed in order to study the changes occurring in the attached boundary layer. The role of the surface roughness in triggering the early transition also deserves further study, as well as a comparison of different roughness heights.

Acknowledgments We acknowledge "Red Española de Surpercomputación" (RES) for awarding us access to the MareNostrum III machine based in Barcelona, Spain (Ref. FI-2015-2-0026 and FI-2015-3-0011). We also acknowledge PRACE for awarding us access to Fermi and Marconi Supercomputers at Cineca, Italy (Ref. 2015133120). Oriol Lehmkuhl acknowledges a PDJ 2014 Grant by AGAUR (Generalitat de Catalunya). Ugo Piomelli acknowledges the support of the Natural Sciences and Engineering Research Council (NSERC) of Canada under the Discovery Grant Programme (Grant No. RGPIN-2016-04391). Ricard Borrell acknowledges a Juan de la Cierva postdoctoral grant (IJCI-2014-21034). Ivette Rodriguez, Oriol Lehmkuhl, Ricard Borrell and Assensi Oliva acknowledge Ministerio de Economía y Competitividad, Secretaría de Estado de Investigación, Desarrollo e Innovación, Spain (ref. ENE2014-60577-R).

Compliance with Ethical Standards

Conflict of interests The authors declare that they have no conflict of interest.

Appendix: A Note on the Experimental Measurements

A large scattering in the experimental measurements for the rough cylinder is observed. As in the case of the smooth cylinder, some of these discrepancies might be attributed to the wind tunnel blockage ratio, cylinder aspect ratio, turbulence intensity of the free-stream flow and cylinder end conditions, amongst others (see discussion in [10]). In Table 6, a summary of the experimental conditions of the measurements used for comparison in the present study are summarised.

In the experiments performed by [15], glass paper was used for the surface roughness, although the roughness parameter was not reported. Later, in [62] these results were identified by their corresponding surface roughness parameter. The values reported were uncorrected for wind tunnel blockage. However, the authors referred to different end conditions issues caused by small gaps that might produce some departure from ideal two-dimensional flow conditions.

In [13], a small aspect ratio cylinder of $L_z/D = 3.33$ was used. Yet, in [4] the authors commented on this subject pointing out that for the rough cylinder no differences were found in the models of $L_z/D = 3.33$ and $L_z/D = 6.6$. Two out of the three roughness height used in [13] (i.e. $k_s/D = 1.1 \times 10^{-3}$ and $k_s/D = 4.5 \times 10^{-3}$) were obtained by using emery paper calibrated by pressure drop measurements in a square duct and then comparing

JmlID 10494_ArtID 9866_Proof#1 - 14/10/2017

Table 6 Summary of experiments for the range of Re and roughness parameter of interest

Reference	Re range	L_z/D	L_y/D	k_s/D	Type roughness	$Tu[\%]$	Comments
[15]	$2.5 \times 10^4 - 2.5 \times 10^5$	6.6 (16.8)		$5 \times 10^{-4} - 2 \times 10^{-2}$	Glass paper	–	
[13]	$4 \times 10^4 - 3 \times 10^6$	3.33	16.6	$9 \times 10^{-3} - 1.1 \times 10^{-2}$	Emery paper and spheres	0.7	Corrected for wind tunnel
[4]	$1.5 \times 10^4 - 3 \times 10^5$	3.33	16.6	$7.5 \times 10^{-4} - 3 \times 10^{-2}$	Pyramids	0.45	Uncorrected
[19]	$2.4 \times 10^4 - 2.8 \times 10^5$	6.6–22.9	–	$10^{-3} - 1.2 \times 10^{-2}$	Emery cloth	0.9	Open wind-tunnel
[22]	$5 \times 10^4 - 4 \times 10^5$	6.1	12	$1.8 \times 10^{-3} - 1.23 \times 10^{-2}$	Sand paper	0.5	k/D instead of k_s/D is given

the results to those of [63]. However, a rough calibration was made for the spherical roughness, by comparing the results with those of [15] giving as a result a roughness parameter of $k_s = 0.55d$ (where d is the diameter of the spheres). Uniform pyramids of rhomboid basic area were used as roughness elements in [4] which were calibrated based on the results of [15].

In general, all authors refer to the problem of estimating the effective size of the roughness so the values of k_s/D in most of the measurements might represent a rough estimate (e.g. [4, 16, 19]). For a larger compilation and discussion of different experimental conditions and results the reader is referred to [16].

References

1. Flack, K.A., Schultz, M.P.: Roughness effects on wall-bounded turbulent flows. Phys. Fluids **26**, 101,305 (2014). https://doi.org/10.1063/1.4896280
2. Jimenez, J.: Turbulent flows over rough walls. Ann. Rev. Fluid Mech. **36**(1), 173–196 (2004). https://doi.org/10.1146/annurev.fluid.36.050802.122103
3. Raupach, M.R., Antonia, R.A., Rajagopalan, S.: Rough-wall boundary layers. Appl. Mech. Rev. **44**, 1–25 (1991)
4. Achenbach, E., Heinecke, E.: On vortex shedding from smooth and rough cylinders in the range of Reynolds numbers 6e3 to 5e6. J. Fluid Mech. **109**, 239–251 (1981)
5. Roshko, A.: Experiments on the flow past a circular cylinder at very high Reynolds number. J. Fluid Mech. **10**(3), 345–356 (1961). https://doi.org/10.1017/S0022112061000950
6. Williamson, C.H.K.: Vortex dynamics in the cylinder wake. Ann. Rev. Fluid Mech. **28**(1), 477–539 (1996). https://doi.org/10.1146/annurev.fl.28.010196.002401
7. Bursnall, W., Loftin, L.J.: Experimental investigation of the pressure distribution about a yawed circular cylinder in the critical Reynolds number range. Technical report TN 2463, NACA (1951)
8. Delany, N., Sorensen, N.: Low-speed drag of cylinders of various shapes. Technical report TN 3038, NACA (1953)
9. Lehmkuhl, O., Rodríguez, I., Borrell, R., Chiva, J., Oliva, A.: Unsteady forces on a circular cylinder at critical Reynolds numbers. Phys. Fluids **26**(12), 125,110 (2014). https://doi.org/10.1063/1.4904415
10. Rodríguez, I., Lehmkuhl, O., Chiva, J., Borrell, R., Oliva, A.: On the flow past a circular cylinder from critical to super-critical Reynolds numbers: Wake topology and vortex shedding. International Journal of Heat and Fluid Flow (2015) https://doi.org/10.1016/j.ijheatfluidflow.2015.05.009
11. Schewe, G.: On the force fluctuations acting on a circular cylinder in crossflow from subcritical up to transcritical Reynolds numbers. J. Fluid Mech. **133**, 265–285 (1983)
12. Wieselsberger, C.: New data on the laws of fluid resistance. Technical report TN 84, NACA (1921)
13. Achenbach, E.: Influence of surface roughness on the cross-flow around a circular cylinder. J. Fluid Mech. **46**(2), 321–335 (1971)
14. Szechenyi, E.: Supercritical Reynolds number simulation for two-dimensional flow over circular cylinders. J. Fluid Mech. **70**, 529–542 (1975)
15. Fage, A., Warsap, J.: The effects of turbulence and surface roughness on the drag of a circular cylinder. Technical report. Rand&M 1283, Aeronautical Research Council (1929)
16. Güven, O., Farell, C., Patel, V.C.: Surface-roughness effects on the mean flow past circular cylinders. J. Fluid Mech. **98**(4), 673 (1980). https://doi.org/10.1017/S0022112080000341
17. Shih, W., Wang, C., Coles, D., Roshko, A.: Experiments on flow past rough circular cylinders at large Reynolds numbers. J. Wind Eng. Ind. Aerodyn. **49**, 351–368 (1993)
18. Batham, J.P.: Pressure distributions on circular cylinders at critical Reynolds numbers. J. Fluid Mech. **57**(02), 209 (1973). https://doi.org/10.1017/S0022112073001114
19. Buresti, G.: The Effect of Surface Roughness on the flow regime around circular cylinders. J. wind Eng. Ind. Aerodyn. **8**, 105–114 (1981)
20. Nakamura, Y., Tomonari, Y.: The effects of surface roughness on the flow past circular cylinders at high Reynolds numbers. J. Fluid Mech. **123**, 363–378 (1982). https://doi.org/10.1017/S0022112082003103
21. Ribeiro, J.L.D.: Effects of surface roughness on the two- dimensional flow past circular cylinders II : fluctuating forces and pressures wind section. J. Wind Eng. Ind. Aerodyn. **37**, 311–326 (1991a)
22. Ribeiro, J.L.D.: Effects of surface roughness on the two-dimensional flow past circular cylinders I : mean forces and pressures. J. Wind Eng. Ind. Aerodyn. **37**, 299–309 (1991b)

23. Lee, S.J., Lim, H.C., Han, M., Lee, S.S.: Flow control of circular cylinder with a V-grooved micro-riblet film. Fluid Dyn. Res. **37**(4), 246–266 (2005). https://doi.org/10.1016/j.fluiddyn.2005.05.002
24. Quintavalla, S.J., Angilella, A.J., Smits, A.J.: Drag reduction on grooved cylinders in the critical Reynolds number regime. Exp. Thermal Fluid Sci. **48**, 15–18 (2013). https://doi.org/10.1016/j.expthermflusci.2013.01.018
25. Leonard, A.: Energy cascade in large-eddy simulations of turbulent fluid flows. AdvGeophys **18A**, 237–248 (1975)
26. Yuan, J., Piomelli, U.: Numerical simulations of sink-flow boundary layers over rough surfaces. Phys. Fluids **26**, 015,113 (2014b). https://doi.org/10.1063/1.4862672
27. Nicoud, F., Ducros, F.: Subgrid-scale stress modelling based on the square of the velocity gradient tensor. Flow, Turbul. Combust. **62**, 183–200 (1999). https://doi.org/10.1023/A:1009995426001
28. Jofre, L., Lehmkuhl, O., Ventosa, J., Trias, F.X., Oliva, A.: Conservation properties of unstructured finite-volume mesh schemes for the Navier-Stokes equations. Numer. Heat Transf. Part B: Fund. **54**(1), 53–79 (2014)
29. Trias, F.X., Lehmkuhl, O., Oliva, A., Pérez-Segarra, C.D., Verstappen, R.W.C.P.: Symmetry-preserving discretization of Navier-Stokes equations on collocated unstructured grids. J. Comput. Phys. **258**, 246–267 (2014). https://doi.org/10.1016/j.jcp.2013.10.031
30. Trias, F.X., Lehmkuhl, O.: A self-adaptive strategy for the time integration of Navier-Stokes equations. Numer. Heat Transf. Part B **60**(2), 116–134 (2011). https://doi.org/10.1080/10407790.2011.594398
31. Rodríguez, I., Borrell, R., Lehmkuhl, O., Pérez-Segarra, C.D., Oliva, A.: Direct numerical simulation of the flow over a sphere at Re = 3700. J. Fluid Mech. **679**, 263–287 (2011). https://doi.org/10.1017/jfm.2011.136
32. Scotti, A.: Direct numerical simulation of turbulent channel flows with boundary roughned with virtual sandpaper. Phys. Fluids **18**, 031,701 (2006)
33. Yuan, J., Piomelli, U.: Estimation and prediction of the roughness function on realistic surfaces. J. Turbul. **15**(6), 350–365 (2014a). https://doi.org/10.1080/14685248.2014.907904
34. Yuan, J., Piomelli, U.: Numerical simulation of a spatially developing accelerating boundary layer over roughness. J. Fluid Mech. **780**, 192–214 (2015). https://doi.org/10.1017/jfm.2015.437
35. Borrell, R., Lehmkuhl, O., Trias, F.X., Oliva, A.: Parallel direct Poisson solver for discretisations with one Fourier diagonalisable direction. Comput. Phys. **230**(12), 4723–4741 (2011). https://doi.org/10.1016/j.jcp.2011.02.042
36. Borrell, R., Chiva, J., Lehmkuhl, O., Oyarzun, G., Rodriguez, I., Oliva, A.: Optimising the Termofluids CFD code for petascale simulations. Int. J. Comput. Fluid Dyn. **30**(6), 425–430 (2016). https://doi.org/10.1080/10618562.2016.1221503
37. Aljure, D., Lehmkhul, O., Rodríguez, I., Oliva, A.: Three dimensionality in the wake of the flow around a circular cylinder at Reynolds number 5000. Comput Fluids **147**, 102–118 (2017). https://doi.org/10.1016/j.compfluid.2017.02.004
38. Lehmkuhl, O., Rodríguez, I., Borrell, R., Oliva, A.: Low-frequency unsteadiness in the vortex formation region of a circular cylinder. Phys. Fluids **25**, 085,109 (2013). https://doi.org/10.1063/1.4818641
39. Mansy, H., Yang, P., Williams, D.: Quantitative measurements of three-dimensional structures in the wake of a cylinder. J. Fluid Mech. **270**, 277–296 (1994)
40. Norberg, C.: Ldv measurements in the near wake of a circular cylinder. In: Proceedings of the ASME conference on advances in the understanding of bluff body wakes and vortex induced vibration. Washington (1998)
41. Humphreys, J.S.: On a circular cylinder in a steady wind at transition Reynolds numbers. J. Fluid Mech. **9**(4), 603–612 (1960). https://doi.org/10.1017/S0022112060001341
42. Pope S.B.: Turbulent flows. Cambridge University Press, Cambridge (2000)
43. West, G., Apelt, C.: Blockage and aspect ratio effects on flow past a circular cylinder for $10^4 < Re < 10^5$. Technical Report No. CE 29. University of Queensland, Australia (1981)
44. Bearman, P.W.: On vortex shedding from a circular cylinder in the critical Reynolds number regime. J. Fluid Mech. **37**, 577–585 (1969)
45. Ünal, U., Atlar, M.: An experimental investigation into the effect of vortex generators on the near-wake flow of a circular cylinder. Exp. Fluids **48**, 1059–1079 (2010). https://doi.org/10.1007/s00348-009-0791-6
46. Roshko, A.: On the development of turbulent wakes from vortex streets. Technical Report NACA TR 1191, California Institute of Technology (1954a)
47. Roshko, A.: On the drag and shedding frequency of two-dimensional bluff bodies. Technical Report TN3169, National Advisory Committee for Aeronautics (1954b)
48. Adachi, T.: Effects of surface roughness on the universal Strouhal number over the wide Reynolds number range. J. Wind Eng. Ind. Aerodyn. **69-71**, 399–412 (1997)

JrnlID 10494_ArtID 9866_Proof#1 - 14/10/2017

49. Yarusevych, S., Sullivan, P.E., Kawall, J.G.: On vortex shedding from an airfoil in low-Reynolds-number flows. J. Fluid Mech. **632**, 245 (2009)
50. Yeung, W.: On pressure invariance, wake width and drag prediction of a bluff body in confined flow. J. Fluid Mech. **622**, 321–344 (2009). https://doi.org/10.1017/S0022112008005247
51. Norberg, C.: Interaction between freestream turbulence and vortex shedding for a single tube in cross-flow. J. Wind Eng. Ind. Aerodyn. **23**, 501–514 (1986)
52. Prasad, A., Williamson, C.: The instability of the shear layer separating from a bluff body. Journal of Fluid Mechanics, pp. 375–492 (1997)
53. Rajagopalan, S., Antonia, R.A.: Flow around a circular cylinder structure of the near wake shear layer. Exp. Fluids **38**(4), 393–402 (2005). https://doi.org/10.1007/s00348-004-0913-0
54. Okamoto, T.: Turbulent shear flow behind hemisphere-cylinder placed on ground plane. In: Turbulent Shear Flows 2, pp. 171–185 (1982)
55. Hajimirzaie, S.M., Tsakiris, A.G., Buchholz, J.H.J., Papanicolaou, A.N.: Flow characteristics around a wall-mounted spherical obstacle in a thin boundary layer. Exper. Fluids **55**(6) (2014). https://doi.org/10.1007/s00348-014-1762-0
56. Dutta, R., Nicolle, J., Giroux, A.M., Piomelli, U.: Evaluation of turbulence models on roughened turbine blades. IOP Conf. Ser. Earth Environ. Sci. **49**, 062007 (2016). https://doi.org/10.1088/1755-1315/49/6/062007
57. Townsend, A.A.: The structure of turbulent shear flow. Cambridge University Press, Cambridge (1976)
58. Dong, S., Karniadakis, G.E., Ekmekci, A., Rockwell, D.: A combined direct numerical simulation-particle image velocimetry study of the turbulent near wake. J. Fluid Mech. **569**, 185 (2006)
59. Cantwell, B., Coles, D.: An experimental study of entrainment and transport in the turbulent near wake of a circular cylinder. J. Fluid Mech. **136**, 321–374 (1983). https://doi.org/10.1017/S0022112083002189
60. Ma, X., Karamanos, G., Karniadakis, G.: Dynamics and low-dimensionality of a turbulent wake. J. Fluid Mech. **410**, 29–65 (2000)
61. Ekmekci, A., Rockwell, D.: Effects of a geometrical surface disturbance on flow past a circular cylinder: a large-scale spanwise wire. J. Fluid Mech. **665**, 120–157 (2010). https://doi.org/10.1017/S0022112010003848
62. Schlichting, H. Boundary layer theory, 7th edn. McGraw-Hill Inc., New York (1979)
63. Nikuradse, J.: Laws of Flow in rough pipes. Translation of Stromungsgesetze in rauhen Rohren. VDI-Forschungsheft 361. 1933. Translated to English. Tech. Rep. NACA TM 1292 (1950)

JrnlID 10494_ArtID 9866_Proof#1 - 14/10/2017

AUTHOR QUERIES

AUTHOR PLEASE ANSWER ALL QUERIES:

Q1. (Ivette Rodriguez) has been set as the corresponding author. Please cheque and advise if correct.
Q2. Please check email address for Jorge Chiva, Ricard Borrell and Assensi Oliva if correct.
Q3. Figure 8 contain(s) cutoff text. Otherwise, please confirm if we can retain the current presentation.
Q4. Figures 10,15-20 contains text below the minimum required font size of 6pts. Otherwise, please provide replacement figure file.
Q5. Please provide volume for reference ([52]).